

## **Chronic reduction of store operated $\text{Ca}^{2+}$ entry is viable therapeutically but is associated with cardiovascular complications**

Fang Yu, Raphael Courjaret, Asha Elmi, Ethel Alcantara Adap, Nelson N. Orie, Fawzi Zghyer, Satanay Hubrack, Sajad Hayat, Nidal Asaad, Stefan Worgall, Manikkam Suthanthiran, Vidya Mohamed Ali, Khaled Machaca

### **Item type**

Journal Contribution

### **Terms of use**

This work is licensed under a [CC BY 4.0](https://creativecommons.org/licenses/by/4.0/) license

### **This version is available at**

[https://manara.qnl.qa/articles/journal\\_contribution/Chronic\\_reduction\\_of\\_store\\_operated\\_Ca\\_sup\\_2\\_sup\\_entry\\_is\\_viable\\_therape](https://manara.qnl.qa/articles/journal_contribution/Chronic_reduction_of_store_operated_Ca_sup_2_sup_entry_is_viable_therape)

Access the item on Manara for more information about usage details and recommended citation.

**Posted on Manara – Qatar Research Repository on**

2022-10-01

# Chronic reduction of store operated $\text{Ca}^{2+}$ entry is viable therapeutically but is associated with cardiovascular complications

Fang Yu<sup>1,2</sup>, Raphael Courjaret<sup>1,2</sup>, Asha Elmi<sup>3</sup>, Ethel Alcantara Adap<sup>1</sup>, Nelson N. Orié<sup>4</sup> , Fawzi Zghyer<sup>5</sup>, Satanay Hubrack<sup>1,2</sup>, Sajad Hayat<sup>6</sup>, Nidal Asaad<sup>6</sup>, Stefan Worgall<sup>7</sup>, Manikkam Suthanthiran<sup>8</sup>, Vidya Mohamed Ali<sup>4</sup> and Khaled Machaca<sup>1,2</sup> 

<sup>1</sup>Calcium Signaling Group, Research Department, Weill Cornell Medicine Qatar, Education City, Qatar Foundation, Doha, Qatar

<sup>2</sup>Department of Physiology and Biophysics, Weill Cornell Medicine, New York, NY, USA

<sup>3</sup>College of Health and Life Science, Hamad bin Khalifa University, Doha, Qatar

<sup>4</sup>Anti-Doping Lab Qatar, Doha, Qatar

<sup>5</sup>Medical Program, Weill Cornell Medicine Qatar, Doha, Qatar

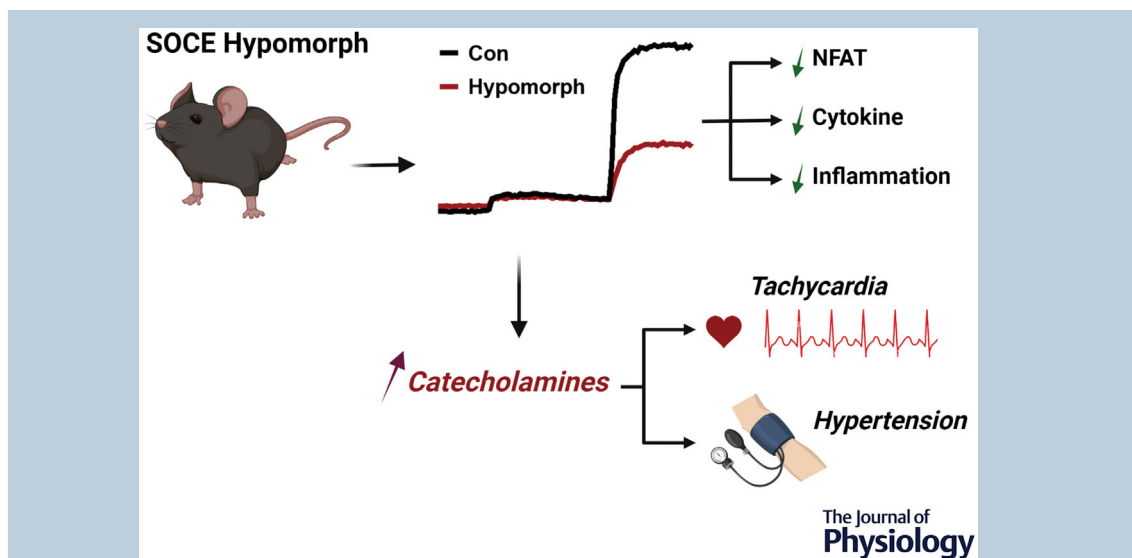
<sup>6</sup>Heart Hospital, Hamad Medical Corporation, Doha, Qatar

<sup>7</sup>Department of Pediatrics, Weill Cornell Medicine, New York, NY, USA

<sup>8</sup>Division of Nephrology and Hypertension, Departments of Medicine and Transplantation Medicine, New York Presbyterian Hospital – Weill Cornell Medical College, New York, NY, USA

Handling Editors: Bjorn Knollmann & Keisa Mathis

The peer review history is available in the Supporting Information section of this article (<https://doi.org/10.1113/JP283811#support-information-section>).



**Abstract** Loss of function mutations in store-operated  $\text{Ca}^{2+}$  entry (SOCE) are associated with severe paediatric disorders in humans, including combined immunodeficiency, anaemia, thrombocytopenia, anhidrosis and muscle hypotonia. Given its central role in immune cell activation, SOCE has been a therapeutic target for autoimmune and inflammatory diseases. Treatment for such chronic diseases would require prolonged SOCE inhibition. It is, however, unclear whether chronic SOCE inhibition is viable therapeutically. Here we address this issue using a novel genetic mouse model (SOCE hypomorph) with deficient SOCE, nuclear factor of activated T cells activation, and T cell cytokine production. SOCE hypomorph mice develop and reproduce normally and do not display muscle weakness or overt anhidrosis. They do, however, develop cardiovascular complications, including hypertension and tachycardia, which we show are due to increased

sympathetic autonomic nervous system activity and not cardiac or vascular smooth muscle autonomous defects. These results assert that chronic SOCE inhibition is viable therapeutically if the cardiovascular complications can be managed effectively clinically. They further establish the SOCE hypomorph line as a genetic model to define the therapeutic window of SOCE inhibition and dissect toxicities associated with chronic SOCE inhibition in a tissue-specific fashion.

(Received 5 September 2022; accepted after revision 23 September 2022; first published online 1 October 2022)

**Corresponding author** K. Machaca: Calcium Signaling Group, Research Department, Weill Cornell Medicine Qatar, Education City, Qatar Foundation, Doha, Qatar. Email: khm2002@qatar-med.cornell.edu

**Abstract figure legend** Summary of the functional and signalling changes in the stromal interaction molecule 1 hypomorph mouse model with associated toxicities.

### Key points

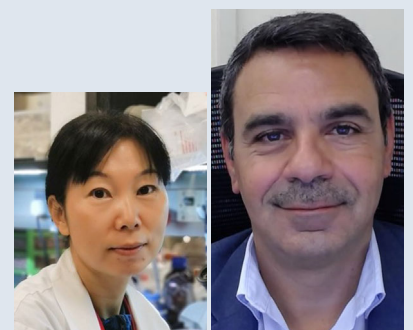
- A floxed stromal interaction molecule 1 (STIM1) hypomorph mouse model was generated with significant reduction in  $\text{Ca}^{2+}$  influx through store-operated  $\text{Ca}^{2+}$  entry (SOCE), resulting in defective nuclear translocation of nuclear factor of activated T cells, cytokine production and inflammatory response. The hypomorph mice are viable and fertile, with no overt defects.
- Decreased SOCE in the hypomorph mice is due to poor translocation of the mutant STIM1 to endoplasmic reticulum–plasma membrane contact sites resulting in fewer STIM1 puncta.
- Hypomorph mice have similar susceptibility to controls to develop diabetes but exhibit tachycardia and hypertension. The hypertension is not due to increased vascular smooth muscle contractility or vascular remodelling.
- The tachycardia is not due to heart-specific defects but rather seems to be due to increased circulating catecholamines in the hypomorph.
- Therefore, long term SOCE inhibition is viable if the cardiovascular defects can be managed clinically.

## Introduction

Store operated  $\text{Ca}^{2+}$  entry (SOCE) is a ubiquitous  $\text{Ca}^{2+}$  influx pathway activated downstream of G-protein- or tyrosine kinase-coupled receptors. In immune cells, antigen binding to T and B cell immunoreceptors activates phospholipase C- $\gamma$ , which hydrolyses phosphatidylinositol-3,4-bisphosphate to generate inositol-1,4,5-trisphosphate ( $\text{IP}_3$ ) and diacylglycerol.  $\text{IP}_3$  binds to  $\text{IP}_3$  receptor  $\text{Ca}^{2+}$  channels on the endoplasmic reticulum (ER) membrane resulting in  $\text{Ca}^{2+}$  release from intracellular stores. The ensuing

depletion of  $\text{Ca}^{2+}$  stores activates a prolonged  $\text{Ca}^{2+}$  influx phase through SOCE that specifically stimulates the  $\text{Ca}^{2+}$ –calmodulin-dependent Ser/Thr phosphatase calcineurin (CaN). CaN dephosphorylates the transcription factor nuclear factor of activated T-cells (NFAT) resulting in its nuclear translocation and expression of cytokines that support immune cell activation (Hogan et al., 2010). Store depletion results in clustering of the ER resident  $\text{Ca}^{2+}$  sensor stromal interaction molecule 1 (STIM1) and its enrichment at ER–plasma membrane (PM) contact sites, where it recruits the  $\text{Ca}^{2+}$ -selective channel Orai1 at the PM

**Fang Yu** is a research assistant professor at Weill Cornell Medicine. Her research focuses on the regulation of store-operated  $\text{Ca}^{2+}$  entry during M-phase. She is also interested in understanding the plasticity of T helper subsets and its function in immune diseases. **Khaled Machaca** is a professor of physiology and biophysics at Weill Cornell Medicine and the senior associated dean for research, innovation and commercialization at Weill Cornell Medicine Qatar. The Machaca Lab studies signalling pathways regulating cellular differentiation under physiological and pathophysiological conditions with a focus on  $\text{Ca}^{2+}$  signalling.



and gates it open through direct physical interaction, resulting in  $\text{Ca}^{2+}$  influx that activates downstream effectors (Prakriya & Lewis, 2015).

Loss of function (LOF) mutations in either STIM1 or Orai1 in humans cause combined immuno-deficiency (CID), autoimmune haemolytic anaemia and thrombocytopenia, muscle hypotonia, and anhidrotic ectodermal dysplasia (Lacruz & Feske, 2015; Vaeth et al., 2020). CID is associated with severe bacterial, viral, and fungal infections early in life resulting in hospitalization and often requiring hematopoietic stem cell transplantation (Picard et al., 2009). Interestingly, different levels of SOCE are needed to support the function of distinct T cell subsets. Effector T cells, such as Th1 and Th17 cells, require strong  $\text{Ca}^{2+}$  signals to support inflammatory cytokine production, whereas follicular T helper cells and B cells that mediate humoral and cellular immunity require relatively smaller SOCE (reviewed in Vaeth et al., 2020). These differential thresholds support a therapeutic window targeting SOCE to inhibit inflammation without affecting other immune functions. In contrast to the immune system where the SOCE dose dependence has been well studied, the specific SOCE requirements in other tissues such as muscle and exocrine glands that exhibit pathologies in the absence of SOCE are less well defined. This is an important issue to resolve if SOCE is to be targeted therapeutically as these requirements would define tissue-specific pathologies.

Given its immunomodulatory role, there is significant interest in pharmacological inhibition of SOCE to treat autoimmune and inflammatory diseases such as psoriasis, acute pancreatitis, rheumatoid arthritis, multiple sclerosis and asthma (Stauderman, 2018). However, inhibition of SOCE raises important safety concerns given the ubiquitous expression of STIM and Orai proteins, the established role for SOCE in skeletal muscle and exocrine glands, and complications from chronic immunosuppression such as those observed in patients on calcineurin inhibitors after organ transplantation (Hartono et al., 2013). This highlights the need for animal models to study the effects of SOCE inhibition throughout development. Several knockout mouse models of STIM1 and Orai1 have been generated. Global STIM1/Orai1 knockouts are lethal postnatally (Gwack et al., 2008; Oh-Hora et al., 2008; Vig et al., 2008), and are thus not informative in terms of potential complications from SOCE inhibition. Furthermore, several investigators have developed tissue-specific SOCE knockouts, but these mouse lines offer limited information as to the global toxicity of SOCE inhibition at various stages of development. Furthermore, it is likely that transcriptional remodelling is different following knockout of SOCE *versus* its partial inhibition, which would lead to disparate complications.

Here, we report our development of a novel SOCE hypomorph mouse model by genetically altering STIM1's structure, resulting in significant inhibition of SOCE, cytokine production by T cells, and NFAT nuclear translocation. Hypomorph mice develop and reproduce normally, thus allowing the dissection of pathologies associated with chronic SOCE inhibition in a tissue-specific fashion in an effort to define the therapeutic window of SOCE inhibition.

## Methods

### Ethical approval

All animal procedures were approved by the Institutional Animal Care and Use Committee (IACUC) at the WCM-Q (Protocol No. 2014-0043). The authors understand and the study conforms to the principles and regulations of *The Journal of Physiology*.

The mouse strains used in this study include wild-type (WT) C57Bl6; the conditional STIM1 knockin strain (ConKI, generated by Ozgene, Bentley, Australia), which expresses WT STIM1; the STIM1 knockin strain (KI, generated by Ozgene), which expresses the long STIM1 isoform and results in decreased SOCE; the STIM1 T cell-specific knockout strain (cKO); and the heart-specific STIM1 hypomorph strain ( $\alpha\text{MHC-cre}$ ). STIM1<sup>fl/fl</sup>-CD4-Cre conditional knockout mice (cKO) maintained on C57BL/6J background were previously described (Yu et al., 2019). C57BL/6J (JAX stock no. 000664) and B6.FVB-tg(Myh6-Cre)2182Mds/J (JAX stock no. 011038) (Agah et al., 1997) mice were purchased from The Jackson Laboratory (Bar Harbor, ME, USA). All mice were maintained under a 12:12 h light-dark cycle in a temperature-controlled room ( $\sim 22^\circ\text{C}$ ) with free access to food and water. Male mice were used in most studies except for the rotarod, RNA seq, and heart rate measurements for the  $\alpha\text{MHC-cre}$  hypomorph experiments where both sexes were used. Mice ranged in age between 3 and 6 months. Mice were put on either standard chow diet (SCD, 15% energy by fat), or high-fat diet (HFD, 60% energy by fat) as indicated. Adult mice were used in all experiments.

### Generation of the STIM1 hypomorph knockin mouse

Targeting vectors (RP23-93K12 and RP23-32M3) were designed to conditionally replace exons 10–12 of the C57BL/6J STIM1 allele with mutant allele containing 10 alanine substitutions of C-terminal serine or threonine residues followed by a proline, except for serine 602. The targeting construct contained a floxed region consisting of a WT minigene cassette of exons 10–12, followed downstream by a FRT-flanked phosphoglycerine kinase (PGK)

promoter driven neomycin (Neo) cassette. A knockin element downstream of the floxed region duplicated exons 10–12 and incorporated the 10 S/T to Ala substitutions. The targeting vector was electroporated into BL6\_Bruce4 ES cells and cells that had undergone homologous recombination were selected in the presence of G418 (Kontgen et al., 1993). After confirmation of integration of the targeting vector by Southern blot, positive ES cells were expanded and injected into C57BL/6J blastocysts and chimeras crossed with C57BL/6J mice. The PGK-neomycin cassette was deleted by crossing with C57BL/6 ACTB-FLPe mice (Ozgene) to create a conditional knockin potential line (Con-KI). Subsequent breeding with Cre mice (Ozgene ROSA26 Transgenic Cre deleter mice) generated the STIM1 hypomorph-KI mouse. The Con-KI mouse was used as the WT control for STIM1 hypomorph-KI mouse in experiments. STIM1 hypomorph-KI mice and ConKI mice were maintained by genotyping PCR using primer pairs: 5'-GTTTCCAGATTGTCAATAACCCCG-3' and 5'-CTTTCCTAGTTATCTTCCCAACTGC-3' for WT; 5'-GTAGGTGTCATTCTATTCTGGGGG-3' and 5'-CAATCTCCTCATCCATGTCATCCA-3' for ConKI; 5'-GCAATGCTAATGCCATCCTTAGAG-3' and 5'-GGAGCCAGATATTGCAAAGAAAGG-3' for KI. Heart-specific KI mice ( $\alpha$ MHC-Cre) and littermate WT control mice were generated by breeding ConKI mice with B6.FVB-Tg(Myh6-Cre)2183Mds mice, and the genotypes were confirmed by PCR. All animals were bred and maintained at the Weill Cornell Medicine Qatar (WCMQ) pathogen-free animal facility.

### Mouse telemetry

Mice were anaesthetized with isoflurane (4% induction, 2% maintenance) administered with a precision vaporizer. The level of anaesthesia by isoflurane was frequently monitored through the operation (every 5–10 min) by testing nociceptive withdrawal to ensure that the animal is fully anaesthetized. If the level of anaesthesia appeared incomplete, the percentage of isoflurane in the inhaled oxygen was increased. A radio telemeter probe (HD-X11, Data Sciences International (DSI, New Brighton, MN, USA)) was implanted in the left common carotid artery to monitor blood pressure, ECG, and body temperature. Mice were monitored until they were capable of purposeful movement following cessation of anaesthesia and placed in clean cages with moistened food. Signals were recorded using a receiver (RPC-1; DSI) connected to a data acquisition system (IOX2; EMKA Technologies, Paris, France). The data were collected continuously for up to a week at a sampling rate of 1 kHz. Continuous digital recordings were analysed offline using the ECG-auto, version 1.5.12.22

(EMKA Technologies). Telemetric data were scanned using software by blinded observers to measure heart rate variability (HRV) parameters. In brief, ECG signals were digitally filtered between 0.1 and 1000 Hz and analysed manually to detect arrhythmias identified by RR intervals two times greater or smaller than the mean, and then quantified. RR intervals were calculated from nocturnal ECG recordings. HRV was analysed similarly on the same recordings. For HRV analyses, the RR values not included between  $RR \pm 2$  SD (95.5% confidence intervals) were removed from the analyses. They were not replaced by any averaged or interpolated beat. The indexes used were the mean RR interval and standard deviation of the normal-to-normal interval (SDNN), which reflects total autonomic variability. Mice were euthanized by CO<sub>2</sub> inhalation at the end of experiments.

### Papain-induced inflammation model

Intranasal papain administration for three consecutive days is a model of innate immune-mediated type 2 airway inflammation (Kabata et al., 2020). ConKI and KI mice (12 weeks old) were anesthetized by 2.5% isoflurane inhalation followed by intranasal administration of 30  $\mu$ l of either papain in phosphate-buffered saline (PBS; 1mg/ $\mu$ l) or PBS on days 1, 2 and 3. Mice were euthanized at day 7 by a rising concentration of CO<sub>2</sub> inhalation, lungs were inflated with 4% paraformaldehyde at 25 cmH<sub>2</sub>O for 16 h, and 5 mm paraffin sections were stained with haematoxylin and eosin (H&E). Histological scoring for inflammation was performed based on cellular infiltration in the alveolar parenchyma away from major vessels, the perivenular regions, and the bronchoarterial regions using a 0–3 severity score. A score of 0 indicates no inflammatory cells, a score of 1 represents occasional cuffing by inflammatory cells, a score of 2 indicates a thin layer (1–5 cells thick) of inflammatory cells, and a score of 3 indicates a thick layer (more than 5 cells thick) of inflammatory cells. Combined grading was based on the most severely inflamed section on each slide.

### Rotarod assay

The motor coordination of 7- to 8-week-old male and female mice were tested on a rotarod. Subjects were tested for motor coordination and learning on an accelerating rotarod (Ugo Basile, Stoelting Co., Wood Dale, IL, USA). For the first test session, mice were given three trials, with 45 s between each trial. Two additional trials were given 48 h later. Number of revolutions per minute was set at an initial value of 3, with a progressive increase to a maximum of 30 rpm across 5 min (the maximum trial length). Measures were taken for latency to fall from the top of the rotating barrel. The rotarod assay was performed at



the UNC Carolina Institute for Developmental Disabilities (CIDD), Mouse Behavioral Phenotyping Core following outcrossing of the KI and ConKI lines.

### HRV analyses

HRV analyses were performed on telemetry data using the DSI Ponemah program (Version 6.5). For analysis in the frequency domain, ECG data from each animal were interpolated at 50 Hz using the quadratic method with a tolerance of 50 ms. Furthermore, data of 1 min duration was detrended and multiplied by a Hanning window with overlapping sub-series set to 2 to meet the requirements for performing a discrete fast Fourier transform (DFT). The squared magnitudes of the DFT were then averaged to form a power spectral density of the beat interval time series computed by use of a modified averaged periodogram set to max. In the time domain, the reporting period was set to 1 h with outlier removal set at a maximum of 2 standard deviations and pNN at 6 ms. Root mean square of successive differences (RMSSD) and pNN6 (the percentage of normal consecutive R-R intervals differing by > 6ms) reflect parasympathetic tone, whereas SDNN reflects overall HRV. Low frequency reflects sympathetic activity whereas the high frequency domain reflects parasympathetic activity.

### Non-invasive electrocardiography

ECGs were detected in conscious mice with the ECGenie platform (Mouse Specifics Inc. Framingham, MA, USA) and analysed using the EzCG analysis software (Mouse Specifics Inc.). The cardiac electrical activity was recorded non-invasively using footpad electrodes. For each mouse, intervals and amplitudes were evaluated from continuous recordings of at least 15 ECG signals. Peak detections were used to calculate the heart rate (HR). The software plots its interpretation of P, Q, R, S and T for each beat so that unfiltered noise or motion artifacts are rejected. This is followed by calculations of the mean of the ECG time intervals for each set of waveforms.

### Minipump implantation and blood pressure measurements

Male mice (8 weeks old) were anaesthetized by 2.5% isoflurane inhalation. Depth of anaesthesia was confirmed by verifying an absence of response to ear, toe and/or tail pinch. Osmotic minipumps (Alzet model 2004, Cupertino, CA, USA) loaded with angiotensin II (Ang II, Bachem, Bubendorf, Switzerland) to accomplish an infusion dose of 2 ng/min/g for 2 weeks or an equal volume of vehicle (0.9% saline) were implanted subcutaneously. Mice were monitored until capable of

purposeful movement after anaesthesia, and were housed in individual cages and allowed free access to food and water. The systolic blood pressure (SBP) was recorded by tail-cuff plethysmography (Kent Scientific, Torrington, CT, USA) before (day 0) and on days 7 and 14 after osmotic minipump implantation. Mice were euthanized by a rising concentration of  $\text{CO}_2$  inhalation at the end of the experiments.

### Glucose and insulin tolerance tests

Age matched (~150 days old) male Con-KI and KI animals were used. For glucose tolerance tests (GTT) and insulin tolerance tests (ITT), animals were fasted for 6 h with free access to water prior to the intraperitoneal injection of glucose in form of 10% glucose in PBS solution (2 mg/g for animals on chow diet and 1 mg/g in HFD) or insulin (0.75 mU/g) (Actrapid, Novo Nordisk, Novo Alle, Denmark) were injected intraperitoneally. A droplet of blood was collected at the tip of the tail and glucose levels measured at the indicated times using a glucometer (One Touch Ultra Mini, Lifescan Inc. Malvern, PA, USA). For diet-induced obesity animals were fed a HFD (60 kcal % of fat, D12492, Research Diets, New Brunswick, NJ, USA) and the weight monitored on a weekly basis.

### Vascular reactivity assays

Vessel tension was monitored using a wire myograph system (510A, Danish Myo Technology, Aarhus, Denmark). 3- to 5-month-old normal and angiotensin II (AngII)-induced hypertensive mice were euthanized by a rising concentration of  $\text{CO}_2$  inhalation. The second order mesenteric arteries (MA) were rapidly removed and dissected in ice-cold physiological salt solution (PSS) with the following composition: 119 mM NaCl, 4.7 mM KCl, 1.17 mM  $\text{MgSO}_4$ , 24 mM  $\text{NaHCO}_3$ , 0.026 mM EDTA, 1.17 mM  $\text{NaH}_2\text{PO}_4$ , 5.5 mM glucose and 1.6 mM  $\text{CaCl}_2$ . Each mounted segment (~2 mm) was pre-tensioned to an equivalent of 100 mmHg (13.3 kPa). Vessels were continuously aerated at 37°C and pH 7.4. The normalized luminal diameter of each pressurized segment was obtained automatically according to the manufacturer's instructions and as previously described (Orie et al., 2006). An equilibration period of at least 1 h was allowed during which time vessels were treated with KCl (90 mM) and phenylephrine (10–100  $\mu\text{M}$ ) to ensure full activation and to assess vessel viability. For assessment of vascular function, cumulative concentration–response curves to phenylephrine (PE, Sigma-Aldrich, St Louis, MO, USA), Ang II (Bachem) and U46619 (Tocris, Bristol, UK) were used to evaluate the contractility response; the vasodilatation was assessed by sodium nitroprusside and acetylcholine (ACh, Sigma-Aldrich).

### Sweat test

Mice (14–19 weeks old males) were anaesthetized using 2–3% isoflurane and maintained under anaesthesia for the duration of the experiment using a nose cone. Depth of anaesthesia was confirmed by the absence of response to ear, toe, and/or tail pinch. One hindleg was extended, and the paw cleaned before painting it with 3.5% iodine diluted in ethanol. After drying, the paw was covered with a 10% potato starch solution in castor oil. The paw was photographed after 2, 4, 6, 8 and 12 min to monitor sweating as the development of black sweat dots. Mice were monitored until capable of purposeful movement following cessation of anaesthesia and placed in clean cages with moistened food. The images were analysed using ImageJ (NIH, Bethesda, MD, USA). The total area covered by the dots measured at the 12 min time point was used to estimate the sweating potential of the mice.

### Catecholamine measurements

The quantitative determination of adrenaline and noradrenaline in plasma was performed using enzyme-linked immunosorbent assay (ELISA, Abnova no. KA1877, Taipei, Taiwan) according to the manufacturer's instructions. The signal was detected by a CLARIOstar plus plate reader (BMG Labtech, Ortenberg, Germany). The final results are expressed as ng/ml. The data were analysed using non-linear regression analysis in Prism 9 software (GraphPad Software Inc., San Diego, CA, USA).

### Histology

Descending thoracic aorta tissues were fixed in 10% formalin, underwent a dehydration process with an alcohol series, and were embedded in paraffin wax. Tissues were sectioned into 5  $\mu$ m sections (3 to 5 sections/specimen) and stained with H&E.

### RNA-seq

Tissue samples (at least three biological repeats/group) were collected, homogenized, and total RNA extracted using a RNeasy Kit (Qiagen, Hilden, Germany) and sequenced at WCMQ Genomics Core Facility. Briefly, 400 ng of high integrity (RNA Integrity Number >5) total RNA was depleted of rRNA using the NEBNext rRNA Depletion Kit for Human/Mouse/Rat (New England BioLabs, Ipswich, MA, USA) and was used to generate strand-specific paired-end 100 bp libraries with NEXTflex Rapid Directional RNA-Seq Kit (Bioo-Scientific, Austin, TX, USA). Library quality and quantity were analysed with the Bioanalyzer 2100 (Agilent Technologies, Santa Clara, CA, USA) on a High Sensitivity

DNA chip. The libraries were then pooled in equimolar ratios and sequenced on Illumina NovaSeq 6000 (Illumina Inc., San Diego, CA, USA). Raw sequencing data were analysed by WCMQ Bioinformatics Core Facility. Reads were aligned and quantified with DRAGEN (Dynamic Read Analysis for GENomics) RNA Pipeline 3.6.3 (DRAGEN Host Software Version 05.021.572.3.6.3 and Bio-IT Processor (Ver 0×0 426 1818)) using Mouse Genome build GRCm38 with ensemble gene annotations as the reference genome. The differential expression of genes was performed using DRAGEN Differential Expression 3.6.3 all hosted on Illumina Base-space. The identified genes were further processed via calculating the log<sub>2</sub>-fold change between groups. To identify pathways enriched in the differentially expressed gene (DEG) subsets, DEGs with a 0.585 > log<sub>2</sub>FC or log<sub>2</sub>FC < −0.585 with a corrected *P* value <0.05 were separated into up- or downregulated and analysed using either ENRICH (maayanlab.cloud/Enrichr) (Chen et al., 2013; Kuleshov et al., 2016) or STRING (v 11.5; string-db.org/), with graphical representation using appyters (appyters.maayanlab.cloud/).

### Cell culture

**Generation of mouse embryonic fibroblast cell lines and transfection.** The mouse embryonic fibroblast (MEF) cell lines were generated from the STIM1 hypomorph-KI mice and WT ConKI mice. Briefly, the primary MEFs were prepared from E13.5 embryos. The embryo body was minced and digested in the presence of trypsin. The primary MEFs were cultured in Dulbecco's modified Eagle's medium supplemented with 10% fetal bovine serum (FBS; Thermo Fisher Scientific, Waltham, MA, USA) and 1% penicillin–streptomycin solution. Primary MEFs were immortalized at passage 4 by infected with the recombinant lentiviral vector SV40 supernatant (Capital Biosciences, CIP-0011, Gaithersburg, MD, USA) in the presence of 10  $\mu$ g/ml Polybrene at approximately 50% confluence for 24 h. Cells were continuously grown in the medium 48–72 h after transduction to reach confluency. MEFs (cell line passage 1) were sub-cultured into a 10 cm tissue culture dish. The MEFs were split every 3–4 days for 2 weeks after P1, and then SV40 transformed clones were selected and plated for expansion. Clones were confirmed for SV40 transformation via PCR for DNA fragment of SV40 T-antigen including SV and TA primer pairs, and PCR for the glyceraldehyde 3-phosphate dehydrogenase (GAPDH) fragment was used as control. The primer pairs used are as follows:

5'-TGAGGCTACTGCTGACTCTCAACA-3' and 5'-GCATGACTCAAAAACTTAGCAATTCTG-3' for the SV fragment;

5'-GACCTGTGGCTGAGTTTGCTCA-3' and 5'-GCTT TATTGTGAACCATTTATAAG-3' for the TA fragment; 5'-ACCACAGTCCATGCCATCAC-3' and 5'-TCCACCA CCCTGTTGCTGTA-3' for the GAPDH fragment.

The pDS\_YFP-HA-Orai1 plasmid was a generous gift from R. Lewis (Stanford) (Park et al., 2009), and transient transfections were performed using Lipofectamine 2000 (Thermo Fisher Scientific) according to the manufacturer's protocol.

**T cell culture and stimulation.** For *ex vivo* cultured  $\text{CD4}^{+}$  T cells, total  $\text{CD4}^{+}$  T cells from mouse spleen and lymph nodes were purified using CD4 (L3T4) MicroBeads (Miltenyi Biotec Inc., Gladbach, Germany) according to manufacturer's instruction.  $\text{CD4}^{+}$  T cells were stimulated with plate-bound anti-CD3 (145-2C11) and anti-CD28 (37.51) antibodies and cultured in the neutral condition ( $\text{Th}_{\text{neu}}$ ) in the presence of 50 U/ml human IL-2 or Th1 cell conditions in the presence of 50 IU/ml of hIL-2, 10 ng/ml of IL-12 (PeproTech, London, UK) and 10  $\mu\text{g}/\text{ml}$  anti-IL-4 (11B11, Thermo Fisher Scientific (eBioscience)) as previously described (Yu et al., 2018). Cells were maintained at 37°C in a 5%  $\text{CO}_2$ -humidified incubator. Jurkat cells were obtained from ATCC (Manassas, VA, USA) and cells were cultured in RPMI 1640 medium (Thermo Fisher Scientific) supplemented with 10% heat-inactivated FBS (Sigma), 100 U/ml penicillin and 100  $\mu\text{g}/\text{ml}$  streptomycin. Cells were re-stimulated with 10 ng/ml PMA (phorbol 12-myristate 13-acetate) and 500 nM ionomycin for 5 h in the presence or absence of BTP2 (Tocris) as indicated with 2 mM Monensin (Thermo Fisher Scientific (eBioscience)) during the last 2 h.

### Fluorescence-activated cell sorting analysis

Mouse splenocytes or *ex vivo* cultured Th1 cells were stained with a cocktail of fixable viability dye and antibodies to cell surface markers on ice. Cells were then fixed with 4% paraformaldehyde (PFA) and permeabilized in PBS containing 0.5% Triton X-100 and 0.1% BSA for intracellular cytokine staining. Flow cytometry data were collected with a LSRFortessa cell analyser (BD Biosciences, San Jose, CA, USA) and the results were analysed by using FlowJo V10 software (Tree Star, Ashland, OR, USA). STIM1 (D88E10) Rabbit mAb was obtained from Cell Signaling Technology (Danvers, MA, USA, cat no. 5668). Antibodies specific for mouse CD4 (RM4-5), CD25 (PC61.5), CD44 (IM7), interferon- $\gamma$  (IFN- $\gamma$ ; XMG1.2), CD19 (FJK-16s), B220 (TC11-18H10), CD16/CD32 (93) and Fixable Viability Dye eFluor 506 were purchased from Thermo Fisher Scientific (eBioscience).

### $\text{Ca}^{2+}$ imaging

Thapsigargin (Tg), ionomycin (Ion) and Fura 2-AM were purchased from Thermo Fisher Scientific. For  $\text{CD4}^{+}$  T cells, ion-induced calcium influx was determined by a FlexStation 3 Multi-Mode Microplate Reader (Molecular Devices, San Jose, CA, USA) with simultaneous data collection as described previously (Yu et al., 2019). For MEF cells, Tg-induced calcium influx was detected by the PTI imaging system mounted on an inverted Olympus IX71 microscope (Olympus, Tokyo, Japan) with continuous perfusion. Briefly, MEFs were cultured on glass bottomed 35 mm microplates until reaching 70–80% confluency. Cells were loaded with 1  $\mu\text{M}$  Fura-2 AM in the culture medium and incubated for 25 min at 37°C in an incubator supplied with 5%  $\text{CO}_2$ . Cells were then incubated with  $\text{Ca}^{2+}$ -free Ringer solution (NaCl 120 mM, KCl 5 mM,  $\text{MgCl}_2$  3 mM, Hepes 20 mM, pH 7.4) with 1  $\mu\text{M}$  Tg. SOCE was induced by adding 2 mM  $\text{Ca}^{2+}$  back. Data were acquired using EasyRatioPro1.6 (Horiba, Kyoto, Japan) where individual cells were picked (>20 cells per experiment). Traces plotted represent the mean of 340/380 nm values of samples for different groups. SOCE levels were calculated by subtracting the basal 340/380 values before  $\text{Ca}^{2+}$  addition from the highest value after the  $\text{Ca}^{2+}$  add-back. Data were analysed using Prism (v 9) software.

### Confocal imaging and total internal reflection fluorescence microscopy

MEF cells were cultured on 35 mm glass-bottomed dishes (MatTek, Ashland, MA, USA) at 37°C with 5%  $\text{CO}_2$ . Cells were treated with or without Tg as indicated. After fixation with 4% PFA and permeabilization, cells were stained with either STIM1 (D88E10) Rabbit mAb (Cell Signaling Technology cat. no. 5668) followed by Alexa Fluor 488 conjugated goat anti-rabbit IgG (Thermo Fisher Scientific), or NFATc1 (7A6) Alexa Fluor 488 (Santa Cruz Biotechnology, Dallas, TX, USA) as indicated. 4',6-Diamidino-2-phenylindole (DAPI) staining when applicable was performed using ProLong Gold Antifade Mountant with DAPI (Thermo Fisher Scientific). Confocal images were taken with a Zeiss LSM 880 confocal microscope (Carl Zeiss Microscopy, Oberkochen, Germany) using a Plan Apo  $\times 63/1.4$  oil DIC II objective with pinhole 1AU. All images were processed using Zeiss Zen Black software. Total internal reflection fluorescence (TIRF) imaging was performed on a Zeiss Z1 AxioObserver inverted fluorescence microscope with TIRF slider using an alpha Plan-Apochromat  $\times 63/1.46$  Oil Corr M27 TIRF objective. All images were processed using Zeiss Zen Blue or Black software and analysed by ImageJ. For puncta analyses cutoff for puncta size was 0.0144  $\mu\text{m}^2$  for airyscan based on a resolution of



120 nm and for TIRF 0.09  $\mu\text{m}^2$  based on a resolution of 300 nm.

### Western blots

Protein lysates were prepared as described previously (Yu et al., 2019), and were loaded on NuPAGE Novex 4% to 12% Bis-Tris Protein Gels (Thermo Fisher Scientific). Proteins were transferred onto polyvinylidene difluoride (PVDF) membrane and blocked with 5% milk in Tris-buffered saline–Tween 20; the PVDF was then incubated with primary antibody overnight at 4°C with constant shaking. The PVDF membrane was washed, and secondary antibodies were applied. Proteins that bound to horseradish peroxidase (HRP)-conjugated secondary antibodies were visualized using enhanced chemiluminescence (ECL). The blots were imaged on a Geliance gel imaging systems (Perkin Elmer, Waltham, MA, USA). Primary antibodies used for experiments are STIM1 rabbit polyclonal antibody (Cell Signaling Technology, cat. no. 4916), STIM1 (D88E10) rabbit mAb (Cell Signaling Technology, cat. no. 5668) and  $\beta$ -actin (C4) mouse monoclonal antibody (Santa Cruz Biotechnology, cat. no. sc-47 778). Both HRP-conjugated goat anti-rabbit-IgG and goat anti-mouse-IgG antibodies were purchased from Jackson ImmunoResearch Laboratories (West Grove, PA, USA). ECL detection reagents were obtained from Thermo Fisher Scientific.

### Statistical analyses

Data are presented as means  $\pm$  SD. Groups were compared using Prism 9 software using the statistical tests indicated in the figure legend. Statistical significance is indicated by *P*-values in the figure legends. Statistical significance is indicated in the figures as follows \**P* < 0.05, \*\**P* < 0.01, \*\*\**P* < 0.001.

## Results

### Generation of the STIM1 knockin hypomorph mouse

Given our interest in understanding the role of STIM1 phosphorylation, we generated a floxed conditional knockin mouse line that encodes WT STIM1, flanked by loxP sites, and followed by a non-phosphorylatable STIM1 mutant where all 10 residues that match the extracellular signal-regulated kinase/cyclin-dependent kinase phosphorylation consensus were mutated to alanine (10A mutant) (Fig. 1A, ConKI). We refer to this line as the conditional knockin or control (ConKI or Con), as it expresses WT STIM1 protein (Fig. 1B and C). We designed our strategy for homologous recombination to have the transgene replace endogenous exon 10, while

leaving in the genome exons 11 and 12 (Fig. 1A, KI). Serendipitously, Cre-dependent excision resulted in the exposure of a cryptic splice donor site within the recombinant exon 12 before the stop codon that spliced in frame to the acceptor site within the endogenous exon 11 (Fig. 1A, KI). This splicing event resulted in the expression of a longer chimeric STIM1 protein (Fig. 1B and C). The genomic structures outlined in Fig. 1A for the ConKI and KI strains as well as that for the C57Bl6 strain (WT) were confirmed by PCR (Fig. 1D) and sequencing of the KI. The cryptic splicing in the KI strain resulted in the expression of a longer chimeric STIM1 that ends at residue I661 followed by the insertion of an Ala residue and continuing with a duplication of the STIM1 C-terminal end from residue P493 to the end of the protein (Fig. 1B, KI).

We isolated primary CD4 T cells from the spleen and confirmed by western blot the expression of only WT STIM1 in the Con strain and only the longer STIM1 chimera in the KI strain (Fig. 1C). Kidney tissue from the ConKI, KI and a heterozygous strain confirm the expression of the WT and the long STIM1 chimera as expected (Fig. 1E).

### STIM1 KI line is a loss of function hypomorph with defective cytokine production

Expression of the long STIM1 chimera in primary T cells from KI mice resulted in significant inhibition of SOCE; SOCE was  $64.2 \pm 2.5\%$  smaller than in ConKI cells (Fig. 1F). We further analysed SOCE from a mouse line where STIM1 was knocked out only in T cells (cKO) to obtain the lower SOCE limit in the complete absence of STIM1 (Fig. 1F). We observed a residual SOCE in cKO cells that is significantly smaller than in KI cells (Fig. 1F). Hence, we refer to the KI line as hypomorph given the partial loss of SOCE, which is presumably due to defective function of the long STIM1 chimeric protein (see below).

A potential explanation for the smaller SOCE in the KI is that the long chimeric STIM1 protein is not stable, leading to its degradation. This, however, is not the case, as the levels of STIM1 are comparable in ConKI and KI cells, whereas STIM1 is lost in cKO cells as detected by flow cytometry (Fig. 2A). Furthermore, and in contrast to the cKO line, we did not observe any splenomegaly in the STIM1 KI line (Fig. 2B), arguing against major disruption of immune cell homeostasis.

To further test the effect of SOCE inhibition in the hypomorph on immune cell development, we performed a differential blood cell count and observed no differences in the levels or parameters of either red blood cells or platelets (Table 1). Therefore, despite significant SOCE inhibition in these mice, we did not detect the anaemia or thrombocytopenia described in patients with

LOF mutations in STIM1 or Orai1. Furthermore, no statistically significant differences in the numbers of white blood cells were observed, although there was a trend toward lower white blood cell count in the KI (Table 1). These results are consistent with data from patients with Orai1 or STIM1 mutations, and mice with lineage-specific knockout of STIM1 or Orai1, where no effects on total lymphocyte, neutrophil, basophil or eosinophil levels were noted (Feske et al., 2015). We did, however, observe a significant increase in the percentage of monocytes (Fig. 2C and Table 1). Although absolute monocyte count

trended up in the hypomorph, it did not reach statistical significance (Fig. 2C).

We further assessed the levels of  $\text{CD4}^+$  T cells,  $\text{CD8}^+$  T cells,  $\text{CD4}^+\text{CD25}^+$  T cell subsets and B cells in both the ConKI and KI lines. The percentages of  $\text{CD4}^+$  T cells and  $\text{CD8}^+$  T cells were similar but the percentage of  $\text{CD4}^+\text{CD25}^+$  was higher in the KI, while  $\text{CD19}^+$  B cells were lower in the KI compared to ConKI (Fig. 2D). The increase in  $\text{CD4}^+\text{CD25}^+$  subset in the hypomorph is opposite to findings from patients with homozygous mutations in STIM1 or Orai1 and from T cell-specific

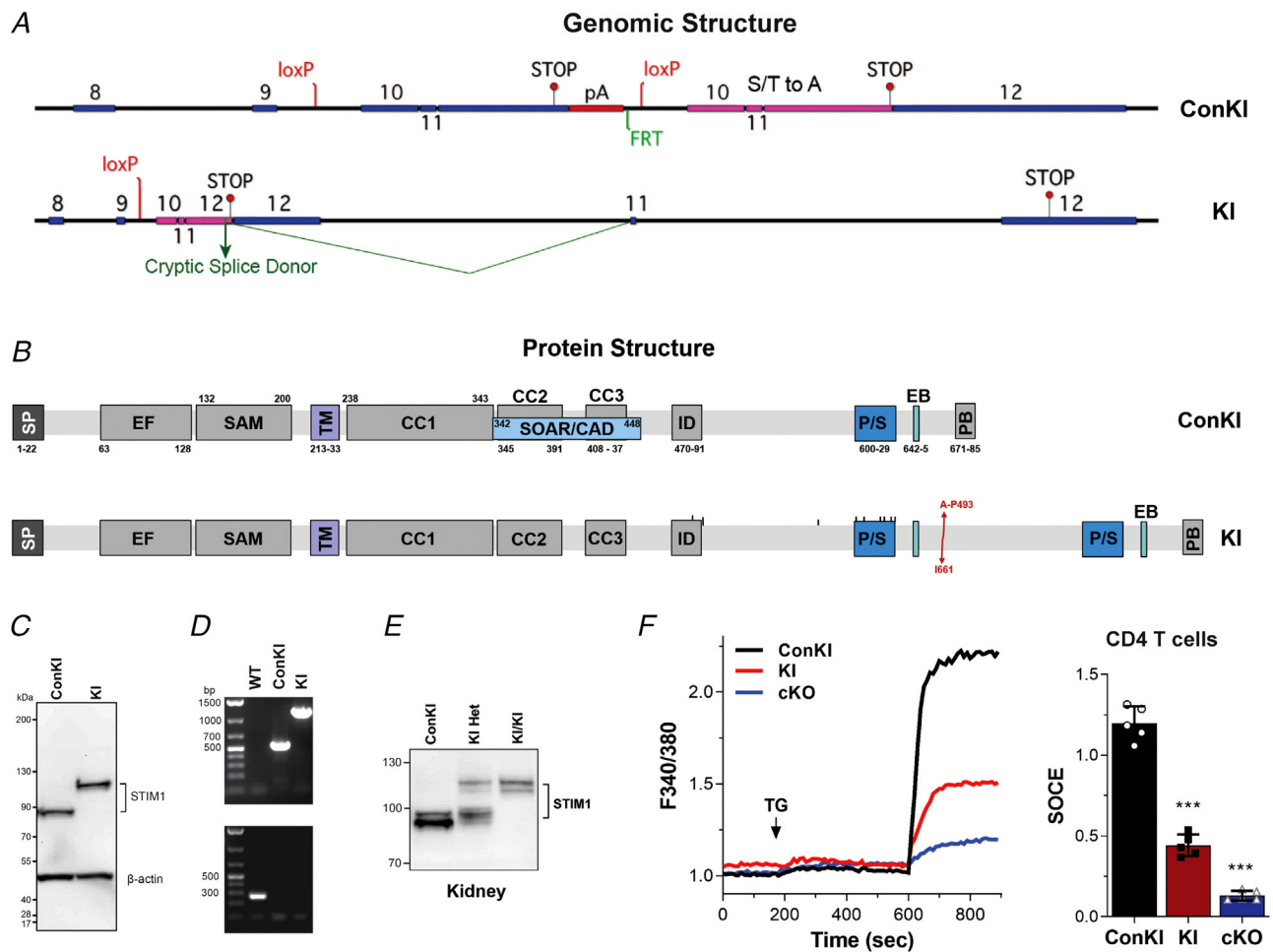


**Figure 1. Generation of the STIM1 hypomorph mouse line**

**A**, organization of the STIM1 genomic locus in the conditional knockin (ConKI) and the hypomorph (KI) lines. **B**, STIM1 protein products in ConKI and KI. The different STIM1 domains are shown: signal peptide (SP), EF-hand (EF), SAM domain (SAM), transmembrane domain (TM), coiled coils 1 (CC1), 2 (CC2) and 3 (CC3), SOAR/CAD domain which binds to and gates Orai1 (SOAR/CAD), inactivation domain (ID), Pro/Ser rich domain (P/S), EB1 binding domain (EB), and polybasic domain (PB). The S/T to A mutated residues are indicated by the bars in the KI. **C**, western blot of splenocyte lysates from ConKI and KI mice using STIM1 and  $\beta$ -actin antibodies. **D**, genotyping PCR with specific primers to confirm homozygosity in the ConKI and KI strain compared to wild-type C57BL/6. **E**, western blot of STIM1 on kidney tissue from control (ConKI), heterozygous and homozygous KI mice. **F**, left panel, example traces from the  $\text{Ca}^{2+}$  re-addition assay from T cells from ConKI, KI and cKO animals.  $\text{Ca}^{2+}$  stores were depleted using thapsigargin (TG, 1  $\mu\text{M}$ ) in  $\text{Ca}^{2+}$ -free medium followed by  $\text{Ca}^{2+}$  addition (2 mM) to induce SOCE. Right panel, SOCE quantification as the peak  $\text{Ca}^{2+}$  signal from baseline (mean  $\pm$  SD,  $n = 5$ , unpaired  $t$ -test,  $P < 0.0001$  for all two-way comparisons). [Colour figure can be viewed at [wileyonlinelibrary.com](http://wileyonlinelibrary.com)]

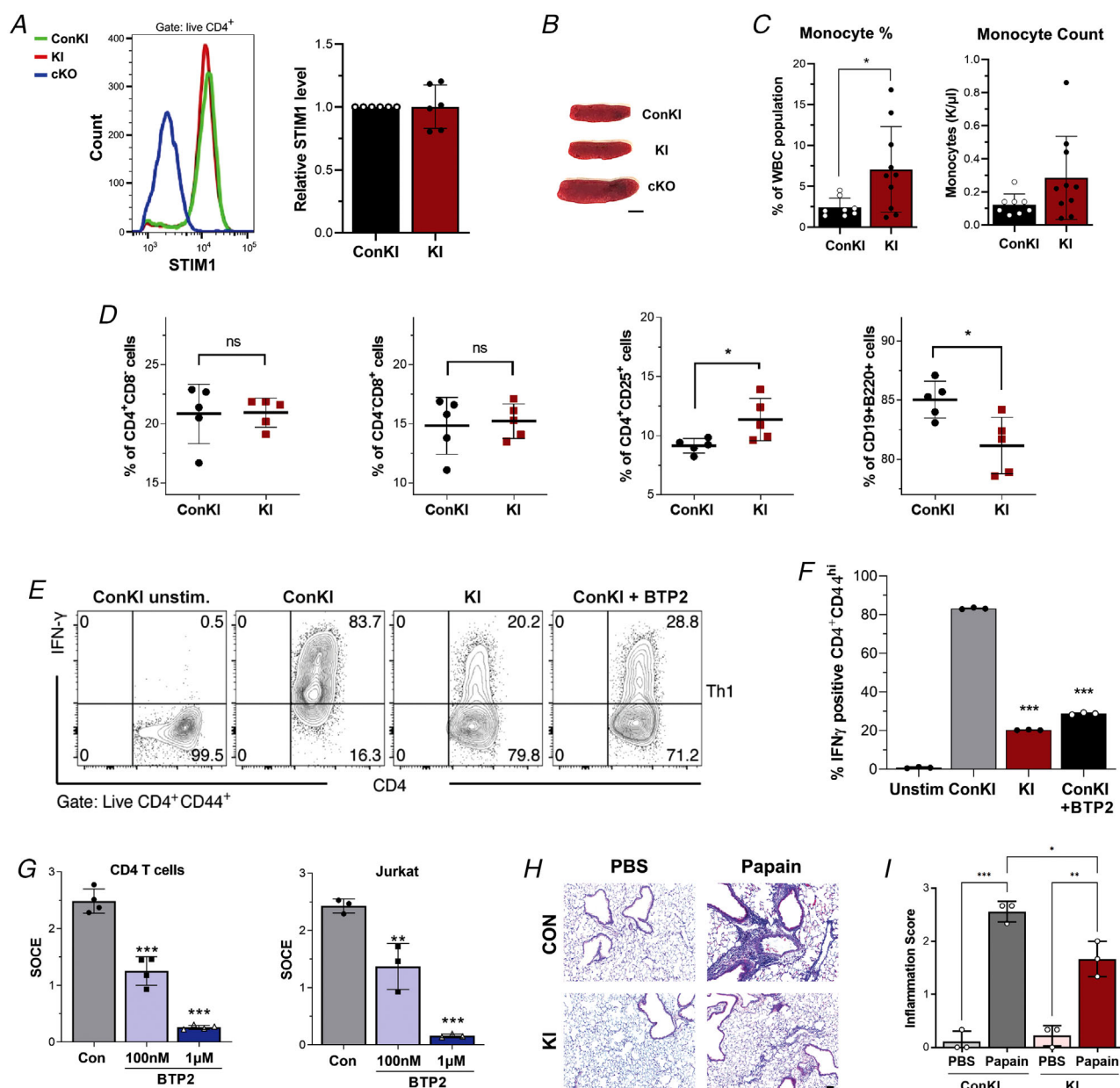


**Figure 2. STIM1 KI line is a loss of function hypomorph**

A, representative flow cytometry traces of STIM1 expression in CD4<sup>+</sup> T cells from ConKI, KI and cKO. Bar graph shows analysis of relative STIM1 expression as the mean fluorescence intensity minus the signal in cKO cells normalized to the ConKI (right panel) (means ± SD, *n* = 6, unpaired *t*-test, *P* = 0.979). B, representative spleens from 3-month-old male ConKI, KI and cKO mice. C, monocyte percent and numbers (means ± SD, *n* = 8–10, Mann–Whitney test, Monocyte percent *P* = 0.0365, Monocyte count *P* = 0.165). D, quantification of T cell subsets and B cells from spleens of ConKI and KI mice (*n* = 5; means ± SD, unpaired *t*-test: CD4<sup>+</sup>CD8<sup>+</sup> *P* = 0.9384; CD4<sup>+</sup>CD8<sup>+</sup> *P* = 0.771; CD4<sup>+</sup>CD25<sup>+</sup> *P* = 0.0305; CD19<sup>+</sup>B220<sup>+</sup> *P* = 0.0158). E, flow cytometry analysis of IFN-γ production from unstimulated or stimulated Th1 cells. BTP2 (100 nM) was added to inhibit SOCE. F, quantification of IFN-γ production under the different conditions (means ± SD, *n* = 3, ANOVA with Tukey correction: ConKI vs. KI *P* < 0.0001, ConKI vs. ConKI+BTP2 *P* < 0.0001). G, dose-dependent SOCE inhibition by BTP2 in stimulated CD4<sup>+</sup> T cells from C57BL/6 mice (means ± SD, *n* = 4, ANOVA with Tukey correction: Con vs. either BTP2 dose *P* < 0.0001) and in Jurkat T cells (means ± SD, *n* = 3, ANOVA with Tukey correction: Con vs. 100 nM *P* = 0.0018, Con vs. 1 μM *P* < 0.0001). H, representative H&E staining of lung tissues from ConKI and KI mice four days following priming with intranasal papain for 3 days to induce airway inflammation. Controls received intranasal PBS. Scale bar is 75 μm. I, inflammation score in the lungs as indicated (means ± SD, *n* = 3, ANOVA with Tukey correction: ConKI PBS vs. Papain *P* = 0.0001, KI PBS vs. Papain *P* = 0.023, Papain ConKI vs. KI *P* = 0.0249). [Colour figure can be viewed at [wileyonlinelibrary.com](http://wileyonlinelibrary.com)]

**Table 1.** Differential analysis of blood cells in the ConKI and KI mice

	ConKI			KI			P
	Mean	SD	n	Mean	SD	n	
RBC ( $\text{M}/\mu\text{l}$ )	11.37	1.163	8	10.89	0.5741	10	0.41
HGB (g/dl)	16.19	1.708	8	15.64	0.7989	10	0.42
HCT %	58.14	6.151	8	55.39	3.491	10	0.32
MCV (fl)	51.18	0.6944	8	50.82	0.8626	10	0.2
MCH (pg)	14.24	0.1408	8	14.36	0.1713	10	0.13
MCHC (g/dl)	27.83	0.4803	8	28.26	0.4169	10	0.08
RDW-CV %	23.58	1.196	8	23.58	0.8066	10	0.88
RET ( $\text{K}/\mu\text{l}$ )	361.5	86.32	8	352.2	39.84	10	0.63
Platelets ( $\text{K}/\mu\text{l}$ )	947.9	95.76	8	893.4	126.7	10	0.24
PDW %	7.375	0.255	8	7.14	0.1647	10	0.05
MPV (fl)	6.313	0.1959	8	6.13	0.1337	10	0.05
P-LCR %	3.975	1.077	8	3.35	0.6078	10	0.28
PCT %	0.5975	0.056	8	0.544	0.0715	10	0.06
WBC ( $\text{K}/\mu\text{l}$ )	5.344	1.639	8	3.909	1.052	10	0.05
Neutrophil %	18.95	9.801	8	12.77	6.203	10	0.08
Lymphocyte %	76.6	9.829	8	77.79	6.676	10	0.92
Monocyte %	2.413	1.159	8	7.08	5.227	10	0.04*
Eosinophil %	1.988	0.7918	8	2.29	1.248	10	0.72
Basophil %	0.05	0.09258	8	0.07	0.116	10	0.78

n is the number of animals for each analyte. Significance was performed using non-parametric t-test with Mann–Whitney correction. Significantly different values are indicated by an asterisk. HCT, haematocrit; HGB, haemoglobin; MCV, mean corpuscular volume; MCH, mean corpuscular haemoglobin; MCHC, mean corpuscular haemoglobin concentration; MPV, mean platelet volume; PCT, plateletcrit, percentage of blood volume occupied by platelets; PDW, platelet distribution width; P-LCR, platelet-large cell ratio; RBC, red blood cells; RDW-CV, red blood cell distribution width – coefficient of variation; RET, reticulocyte count; WBC, white blood cells.

STIM1 knockout mouse lines, where a reduction in cell numbers of both regulatory T cells and invariant natural killer cells was observed (Feske et al., 2015).

The lower SOCE in KI T cells is functionally significant as it was associated with a dramatic decrease in cytokine production following T cells activation (Fig. 2E and F). The inhibition of cytokine production in the KI ( $75.6 \pm 0.05\%$ ) was comparable to pharmacological inhibition of SOCE using BTP2 (Fig. 2E and F). We confirmed that BTP2 dose-dependently blocks SOCE in both primary CD4 T cells and in Jurkat T cells (Fig. 2G). The inhibition in the percentage of T cells responding to stimulation with cytokine production in the hypomorph ( $\sim 75\%$  inhibition) is in line with the observed SOCE reduction ( $\sim 65\%$ ).

The interest in SOCE inhibition clinically is in part to treat inflammatory diseases. Therefore, to test whether hypomorph mice are less susceptible to inflammation, we treated animals with papain to induce inflammation in the lungs. This resulted in a dramatic inflammatory response associated with infiltration of immune cells in the lungs of ConKI animals (Fig. 2H, CON), but not in KI lungs (Fig. 2H, KI). The inflammation score is significantly reduced in hypomorph as compared to control lungs from papain-treated animals (Fig. 2I). This shows that the level

of SOCE inhibition attained in the hypomorph is sufficient to blunt a pathogenic inflammatory response.

### Defective STIM1 activation in the hypomorph

To better understand the defect underlying the decreased SOCE in the STIM1 hypomorph, we generated MEF cell lines from both the ConKI and KI strains. As observed in primary T cells, the KI MEF line expresses the long chimeric STIM1 only and the ConKI MEFs express WT STIM1 at comparable levels (Fig. 3A). Furthermore, KI MEFs have a smaller SOCE as compared to ConKI MEF with a loss of  $65.6 \pm 2.5\%$  of ConKI SOCE (Fig. 3B), without affecting the levels of  $\text{Ca}^{2+}$  in stores (Fig. 3C). This SOCE inhibition is similar to that observed *ex vivo* in T cells (Fig. 2A;  $\sim 64\%$  inhibition) and argues that expression of the long STIM1 results in  $\sim 65\%$  inhibition of SOCE.

To better define the defect in the long chimeric STIM1 underlying a smaller SOCE, we assessed STIM1 puncta formation by immunostaining for endogenous STIM1 followed by TIRF imaging to detect ER–PM junctions enriched in STIM1 at the PM interphase. To control for the



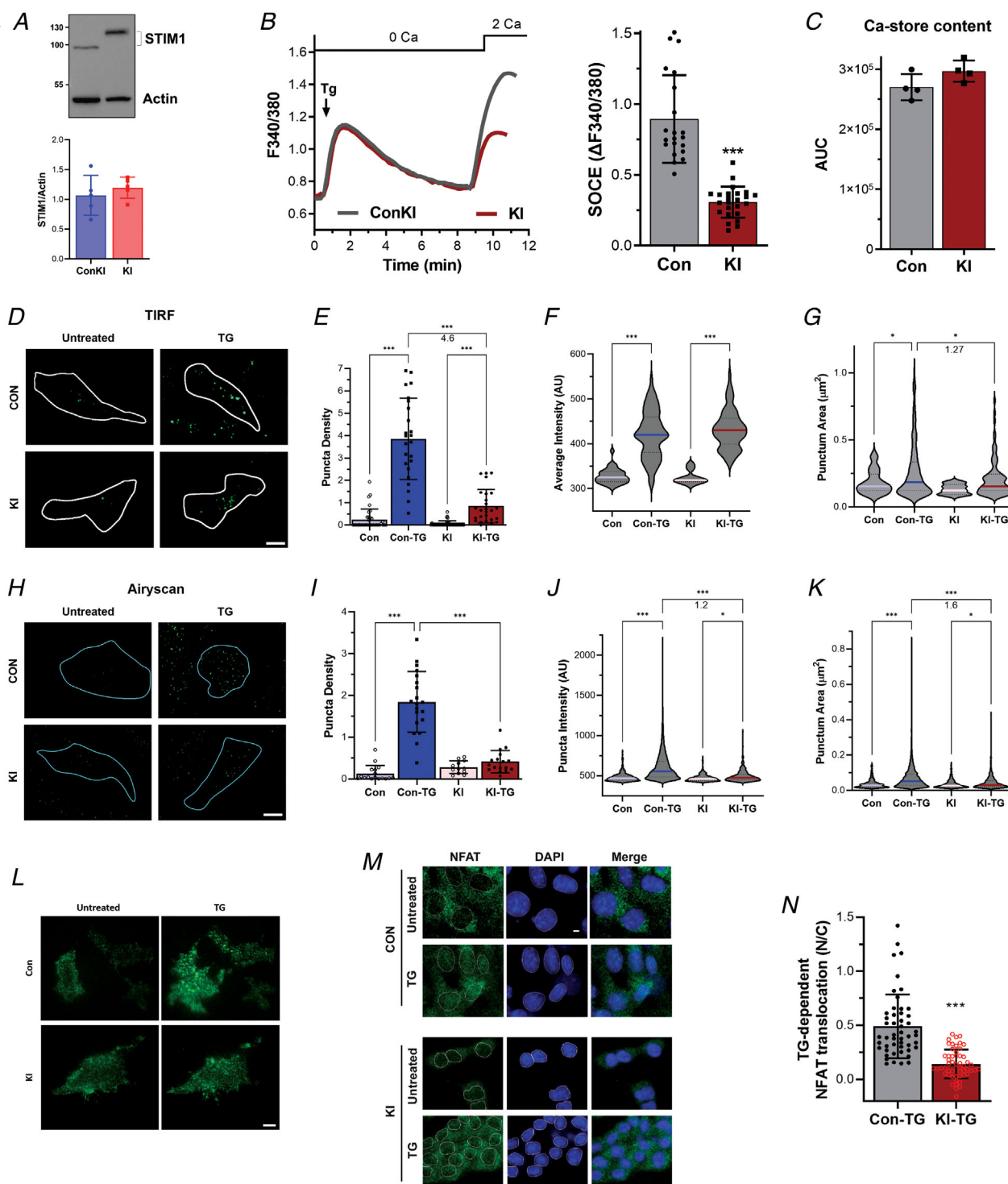


**Figure 3. Defective STIM1 activation in the hypomorph MEFs**

**A**, representative western blot and quantification of STIM1/actin ratio in ConKI and KI MEFs (means ± SD,  $n = 5$ , unpaired  $t$ -test,  $P = 0.47$ ). **B**, representative traces from the  $\text{Ca}^{2+}$  re-addition assay and SOCE quantification in ConKI and KI MEFs.  $\text{Ca}^{2+}$  stores were depleted with thapsigargin (Tg, 1  $\mu\text{M}$ ) in  $\text{Ca}^{2+}$  free Ringer buffer, followed by addition of  $\text{Ca}^{2+}$  (2 mM) to induce SOCE (means ± SD,  $n = 21$ –24, unpaired  $t$ -test,  $P < 0.0001$ ). **C**,  $\text{Ca}^{2+}$  store content measured by releasing store  $\text{Ca}^{2+}$  with ionomycin (5  $\mu\text{M}$ ) and quantifying the area under the curve (AUC) (means ± SD,  $n = 4$ , unpaired  $t$ -test,  $P = 0.11$ ). **D**, representative TIRF images of STIM1 immunostaining before (Untreated) and after store depletion with thapsigargin (1  $\mu\text{M}$ , TG). The footprint of one cell in the field is shown for orientation. Scale bar is 5  $\mu\text{m}$ . **E**, quantification of STIM1 puncta density (means ± SD,  $n = 24$ –40, ANOVA

with Tukey correction: Con vs. Con-TG  $P < 0.0001$ , KI vs. KI-TG  $P < 0.0001$ , Con-TG vs. KI-TG  $P < 0.0001$ ). Con versus KI basal puncta were further analysed using an unpaired  $t$ -test ( $n = 34$ – $40$ ,  $P = 0.0134$ ). *F*, STIM1 puncta intensity (violin plot with the mean and quartiles indicated,  $n = 9$ – $235$ , ANOVA with Tukey correction: Con vs. Con-TG  $P < 0.0001$ , KI vs. KI-TG  $P < 0.0001$ , Con-TG vs. KI-TG  $P = 0.06$ ). *G*, STIM1 puncta area (violin plot with the mean and quartiles indicated,  $n = 9$ – $232$ , ANOVA with Tukey correction: Con vs. Con-TG  $P = 0.02$ , KI vs. KI-TG  $P = 0.23$ , Con-TG vs. KI-TG  $P = 0.01$ ). *H*, representative airyscan confocal images of STIM1 puncta formation detected by immunostaining for STIM1 before (Untreated) and after store depletion with thapsigargin (TG,  $1 \mu\text{M}$ ). The footprint of one cell in the field is shown for orientation. Scale bar is  $5 \mu\text{m}$ . *I*, quantification of STIM1 puncta density (means  $\pm$  SD,  $n = 12$ – $20$ , ANOVA: Con vs. Con-TG  $P < 0.0001$ , KI vs. KI-TG  $P = 0.4222$ , Con-TG vs. KI-TG  $P < 0.0001$ ). *J*, puncta intensity (violin plot with the mean and quartiles indicated,  $n = 363$ – $4142$ , ANOVA with Tukey correction: Con vs. Con-TG  $P < 0.0001$ , KI vs. KI-TG  $P = 0.017$ , Con-TG vs. KI-TG  $P < 0.0001$ ). *K*, puncta area (violin plot with the mean and quartiles indicated,  $n = 363$ – $4142$ , ANOVA with Tukey correction: Con vs. Con-TG  $P < 0.0001$ , KI vs. KI-TG  $P = 0.02$ , Con-TG vs. KI-TG  $P < 0.0001$ ). *L*, representative TIRF images of puncta formation after store depletion in YFP-Orai1 overexpressing MEFs. Scale bar is  $10 \mu\text{m}$ . *M*, representative images of NFAT2 immunostaining with Alexa Fluor 488 conjugated anti-NFAT2 antibody with DAPI to stain nuclei in ConKI MEFs before (Untreated) and after store depletion with thapsigargin (TG) in both ConKI and KI MEFs. The nuclear area in the NFAT IF images are outlined to highlight nuclear translocation. Scale bar is  $5 \mu\text{m}$ . *N*, quantification of TG-dependent NFAT nuclear translocation (means  $\pm$  SEM,  $n = 50$ – $53$ , unpaired  $t$ -test,  $***P < 0.001$ ). [Colour figure can be viewed at [wileyonlinelibrary.com](http://wileyonlinelibrary.com)]

specificity of the anti-STIM1 antibody, we confirmed the absence of staining in the STIM1 knockout MEFs that do not express any STIM1 (Oh-Hora et al., 2008). Although we detected faint puncta at rest in the ConKI MEFs, store depletion led to a dramatic increase in puncta density (Fig. 3D and E). In the KI MEFs STIM1 positive puncta at rest were almost completely absent, but store depletion led to a significant increase in puncta density, which was nonetheless 4.6-fold smaller than in TG-treated ConKI cells (Fig. 3D and E). Puncta density was calculated as the percentage of the cell footprint area covered by puncta. Store depletion was also associated with comparable increases in puncta intensity in both MEF lines (Fig. 3F). Puncta area also increased in response to store depletion with a more pronounced increase in ConKI as compared to KI MEFs (1.27-fold higher) (Fig. 3G). These data show that following store depletion the longer STIM1 in the KI is defective in enrichment at ER–PM junctions as the STIM1 positive puncta in the KI are smaller and significantly fewer.

We further analysed STIM1 enrichment in junctions following store depletion using super-resolution airyscan confocal microscopy. Airyscan offers higher resolution than TIRF allowing us to detect smaller puncta, but its  $z$ -axis resolution is poor and thus it does not exclusively detect STIM1 puncta at the PM interphase but would also distinguish puncta deeper into the cell that may not be coupled to Orai1. We observed a similar 4.5-fold decrease in puncta density following store depletion as detected in TIRF in the KI as compared to Con (Fig. 3H and I). Smaller but significant increases in puncta intensity and area were also detected (Fig. 3J and K). These data support the conclusion that the longer STIM1 does not fully activate in response to store depletion resulting in weaker clustering and stabilization at ER–PM junctions, and thus diminished SOCE activation. This could be due either to less efficient unfolding of STIM1 to expose

the CAD/SOAR domain to interact with Orai1 and the poly-basic domain to interact with PM phospholipids, or to the inability of the long STIM1 to translocate from the deep ER to ER–PM junctions. Regardless, SOCE inhibition is due to the chimeric extended STIM1 C-terminal tail and not the Ser/Thr to Ala mutations, as we have previously show that a STIM1 mutant with the identical S/T to A mutations (10A) did not affect SOCE levels in MEFs or primary cells (Hammad et al., 2021; Yu et al., 2021).

To further support the immunofluorescence analyses, we expressed yellow fluorescent protein (YFP)–Orai1 and tested its clustering in response to store depletion (Fig. 3L). Orai1 forms puncta in ConKI MEFs with background diffuse staining, which is expected given its higher expression compared to endogenous STIM1. Orai1 clustering in response to store depletion was less pronounced although detectable in the KI MEFs (Fig. 3L), supporting the weaker translocation of the long chimeric STIM1 to junctions.

The smaller SOCE and weaker clustering of STIM1 in the KI was associated with less cytokine production in stimulated immune cells (Fig. 2E). This predicts weaker activation of CaN and thus diminished NFAT translocation to induce transcription. We quantified endogenous NFAT nuclear translocation using immunostaining (Fig. 3M and N). NFAT translocation in response to store depletion (Tg-dependent) was significantly reduced in KI cells ( $69.6 \pm 3.4\%$ ) as compared to ConKI MEFs (Fig. 3N).

Collectively these data show that the long chimeric STIM1 expressed in the KI strain is functional but activates poorly in response to store depletion due to the extended chimera and not the S/T to A mutations. This STIM1 chimera is defective in its translocation and enrichment at ER–PM junctions, leading to decreased Orai1 recruitment and SOCE activation. This reduces

CaN-NFAT induction and thus the transcriptional programme that triggers immune cells activation.

### Complications in the SOCE hypomorph

The above results establish the KI line as an SOCE hypomorph with significant suppression of SOCE (~65%), T cell cytokine production (~75%) and NFAT nuclear

translocation (~70%). Despite these remarkable reductions, STIM1-KI mice are viable and reproduce normally with similar litter size as compared to the ConKI line and C57Bl6 (Fig. 4A). Therefore, these levels of SOCE inhibition have little effect on fertility and embryonic and postnatal development.

We further tested other pathologies observed in STIM1/Orai1 LOF patients in the hypomorph, including

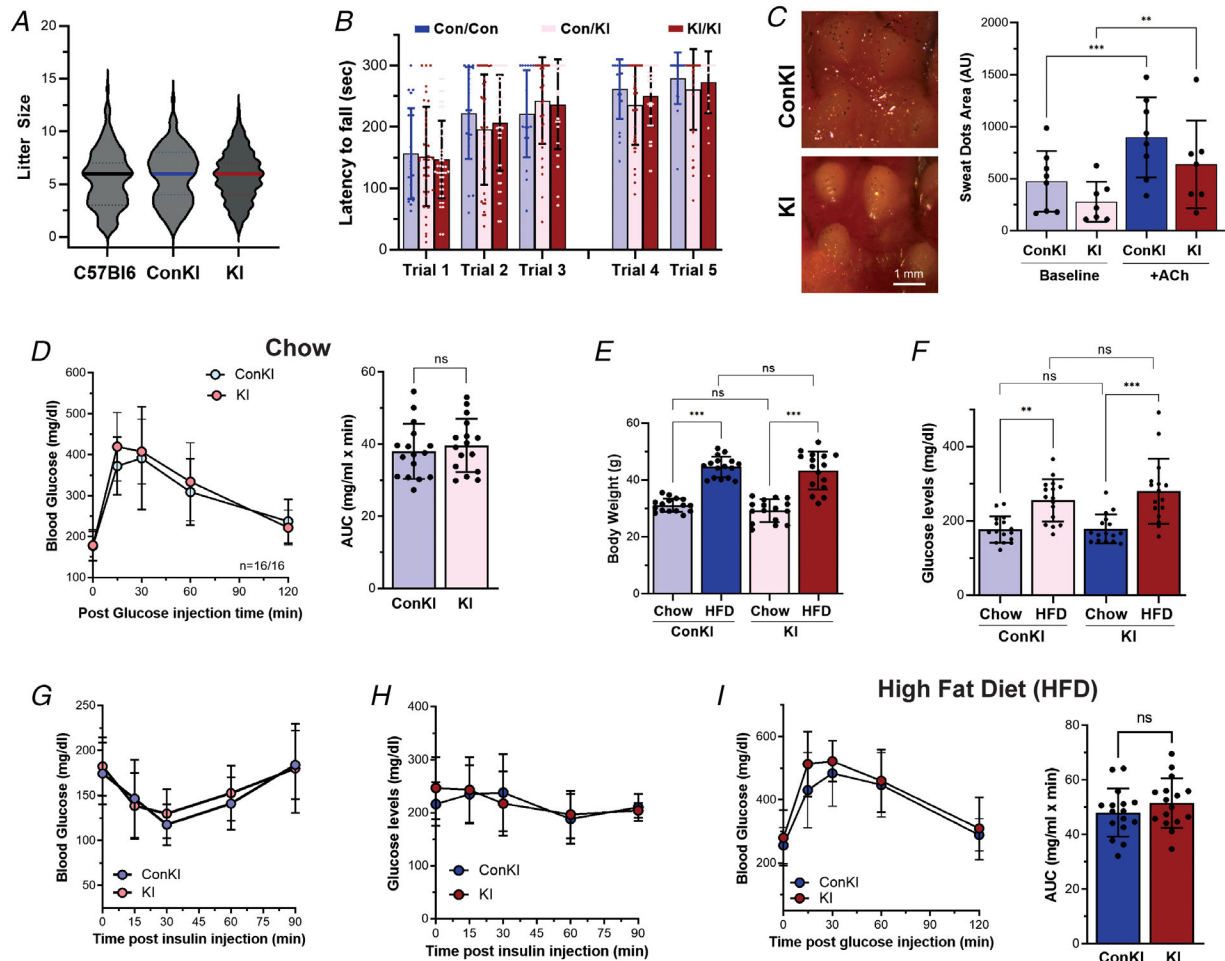


**Figure 4. STIM1 hypomorph mice do not develop diabetes**

A, litter size in the C57Bl6, ConKI and KI strains (violin plot with the mean and quartiles indicated,  $n = 121$ – $203$ , ANOVA with Tukey correction: C57Bl6 vs. ConKI  $P = 0.518$ , C57Bl6 vs. KI  $P = 0.3862$ ). B, latency to fall in the rotarod assay for ConKI, heterozygous (Con/KI) and KI mice (means  $\pm$  SD,  $n = 21$ – $44$ , two-way ANOVA with Tukey correction, not significant). C, left, representative image from the sweat assay. Right, summary of the sweat dot total area before and after stimulation with Ach (means  $\pm$  SD,  $n = 7$ – $8$ , paired  $t$ -test: ConKI vs. ConKI+ACh  $P < 0.0001$ , KI vs. KI+ACh  $P = 0.01$ ; unpaired  $t$ -test: ConKI vs. KI  $P = 0.1535$ , ConKI = Ach vs. KI+ACh  $P = 0.2354$ ). D, glucose tolerance test (GTT) performed on chow-fed animals. Glucose (2 mg/g of body mass) was administered i.p. after reading blood glucose levels at  $t = 0$ . Glycaemia was measured over time and the overall increase in glucose estimated as the area under the curve (AUC, bar graph) (means  $\pm$  SD,  $n = 16$ , unpaired  $t$ -test,  $P = 0.5287$ ). E and F, body weight (E) and basal fasting glucose levels (F) of mice on a chow diet and after 5 weeks on a HFD (means  $\pm$  SD,  $n = 16$ , ANOVA with Tukey correction: weight: ConKI vs. KI  $P = 0.23$ , ConKI vs. HFD  $P < 0.0001$ , KI vs. HFD  $P < 0.0001$ , HFD ConKI vs. KI  $P = 0.41$ ; basal glucose: ConKI vs. KI  $P = 0.99$ , ConKI vs. HFD  $P = 0.002$ , KI vs. HFD  $P < 0.0001$ , HFD ConKI vs. KI  $P = 0.65$ ). G and H, insulin tolerance test (ITT) performed in chow fed animals (G) and HFD (H). Insulin (0.75 mU/g) was injected i.p. on fasting animals after reading baseline glucose. I, GTT performed on HFD-fed animals following i.p. injection of 1 mg/g of glucose (means  $\pm$  SD,  $n = 16$ , unpaired  $t$ -test,  $P = 0.2796$ ). [Colour figure can be viewed at [wileyonlinelibrary.com](http://wileyonlinelibrary.com)]

muscle weakness and anhidrosis. To test for muscle weakness we used the rotarod test with increased rotation speeds and did not observe any difference in the performance of KI as compared to ConKI (Fig. 4B), nor did we observe any sex differences. We further quantified sweating in the two strains using the paw sweating assay and observed a trend toward anhidrosis in the hypomorph although the data did not reach statistical significance (Fig. 4C). These results argue that the residual SOCE in the hypomorph is sufficient to support necessary functions in skeletal muscle and sweat gland with no associated overt pathologies.

### SOCE hypomorph susceptibility to developing diabetes

Because SOCE has been implicated in diabetes development (Estrada et al., 2012; Kono et al., 2018; Mamenko et al., 2016), and because diabetes is a common side effect of chronic immunosuppression (Azzi et al., 2013; Bamgbola, 2016; Chakkerla et al., 2017), we next tested whether hypomorph mice develop diabetes. Glucose tolerance tests show no changes in glucose clearance rates or resting glucose levels between ConKI and KI mice (Fig. 4D), arguing that chronic SOCE inhibition is not sufficient by itself to predispose to diabetes. However, clinically many of the patients on immunosuppressive regimens have associated co-morbidities including metabolic syndrome that are likely to predispose them to diabetes. To explore this possibility, we induced insulin resistance by placing mice on a high fat diet (HFD) for 5 weeks. This resulted in the expected weight gain, which was equivalent in both strains (Fig. 4E). The weight gain was associated with an increase in resting blood glucose levels, which again was similar in both the ConKI and KI strains (Fig. 4F). The increase in blood glucose was due to the mice on a HFD developing insulin resistance (Fig. 4G and H). Insulin injection in animals on a chow diet led to a significant drop in blood glucose levels, which recovered over a 90 min period (Fig. 4G). In contrast, insulin sensitivity was lost in mice on a HFD from both genotypes (Fig. 4H). We did not detect any differences in insulin sensitivity in the KI compared to ConKI strain whether the animals were on chow (Fig. 4G) or HFD (Fig. 4H). We then tested glucose tolerance in KI animals on a HFD and observed no difference in their glucose clearance compared to ConKI animals (Fig. 4I). Therefore, chronic inhibition of SOCE is not sufficient to predispose to diabetes even when insulin resistance is induced.

### Cardiovascular defects in the STIM1 hypomorph

To test for potential cardiovascular pathologies in hypomorph mice, we performed telemetry as it allows long

term recording of ECG and pressure parameters in live mobile mice. The data presented are summaries of recordings over 72–150 h that were replicated in shorter recordings (24 h). Blood pressure (BP) was higher in KI animals as compared to ConKI both during the resting period and at night when the mice are active (Fig. 5A). Mean BP results were mirrored by diastolic BP (Fig. 5B) and to a lesser extent systolic BP (Fig. 5C). Also, interestingly hypomorph mice had a significantly higher heart rate (HR) compared to ConKI during both the day and the night periods (Fig. 5D). We did not detect any significant difference in activity (Fig. 5E) or body temperature (Fig. 5F) between the two strains.

To test whether the increase in BP observed in hypomorph mice could be amplified when hypertension is induced, we implanted mice with slow infusion angiotensin II pumps that led to a dramatic increase in BP (Fig. 5G). Hypomorph animals reach the plateau of maximal BP within 1 week of AngII pump implantation as compared to 2 weeks for control animals (Fig. 5G). Hypertension is typically stabilized either due to vascular remodelling of the arterial wall leading to thickening and thus less responsiveness to hemodynamic needs, or to increased contractility of vascular smooth muscle (VSM) (House et al., 2008), or to altered innervation of the vasculature.

To test for VSM contractility, we isolated mesenteric arterioles from normotensive and hypertensive animals and assessed their contractile responses to agonists. KCl stimulation to depolarize and activate voltage gated  $\text{Ca}^{2+}$  channels led to similar force generation in both ConKI and KI arteries (Fig. 5H), arguing against remodelling of the contractile machinery *per se* in the KI. The arteries isolated had minimal functional endothelium as they did not respond well to acetylcholine administration (Fig. 5I), showing that the contractile response is mainly due to VSM. Sodium nitroprusside, which acts directly on VSM to induce vasodilatation was equally potent in vessels from normotensive and hypertensive ConKI and KI animals (Fig. 5J), arguing that the hypertension sensitivity is not due to defective vasodilatation. We further tested vasoconstriction in response to phenylephrine (PE, Fig. 6A), the thromboxane receptor agonist U46619 (Fig. 6B) and AngII (Fig. 6C). In all cases, we did not observe statistically significant differences in contractile responses between ConKI and KI vessels. This argues against alterations in VSM contractility as the cause for hypertension sensitivity in the hypomorph.

To test for arterial wall remodelling we isolated arteries from ConKI and KI animals and measured the smooth muscle layer thickness, which was similar in both genotypes (Fig. 6D), arguing against dramatic remodelling of the arterial wall as underlying the susceptibility to hypertension in the hypomorph.



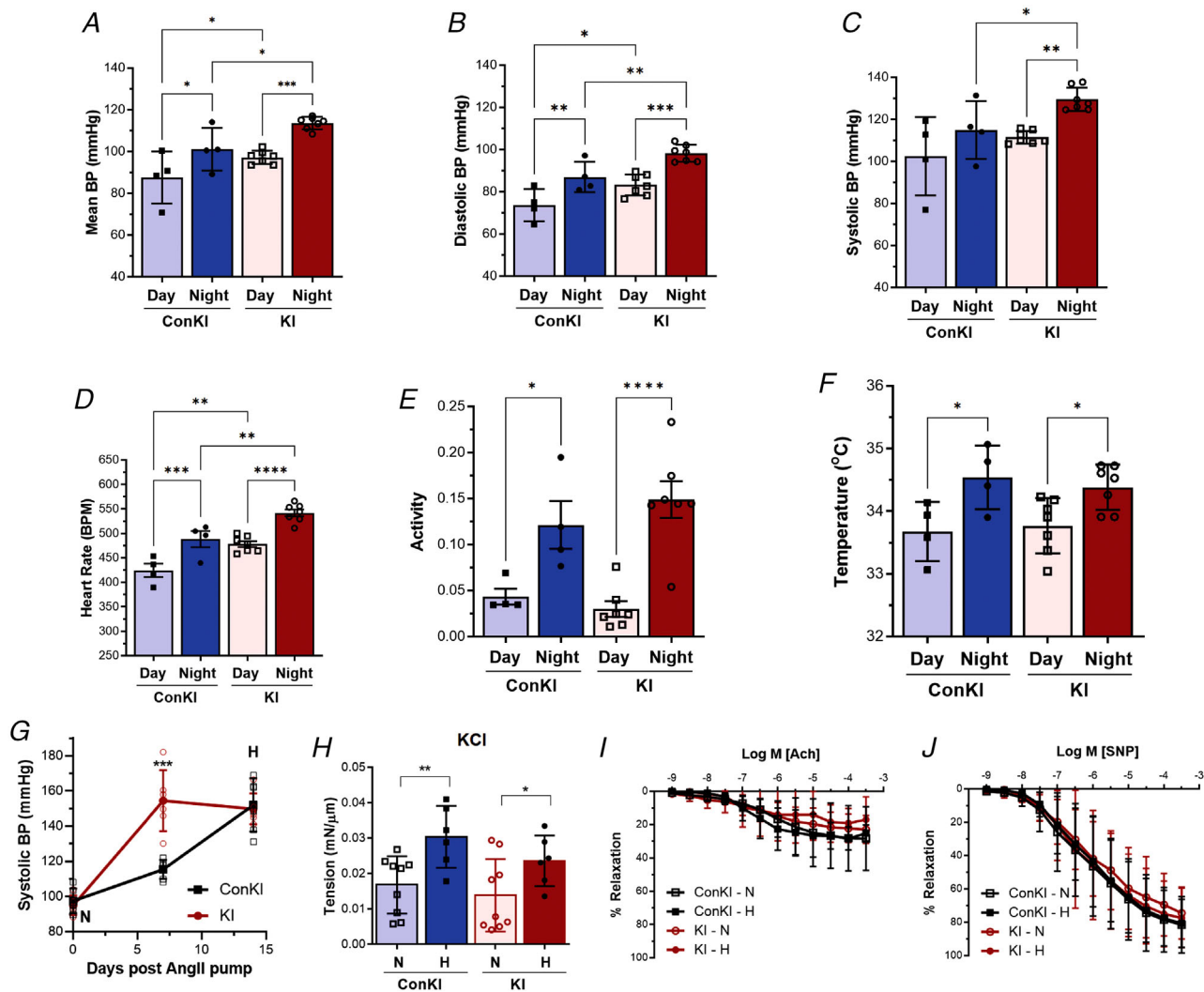


**Figure 5. Cardiovascular pathologies in the STIM1 hypomorph**

A–F, analyses of telemetry recordings, including mean blood pressure (BP, A), diastolic BP (B), systolic BP (C), heart rate (D), activity (E), and body temperature (F) during the day (09.00–14.00 h) and night (21.00–02.00 h) periods in ConKI and KI mice on a light–dark cycle from 06.00 h to 18.00 h (means  $\pm$  SD,  $n = 4–7$ , ANOVA with Fisher's LSD test: mean BP: Con Day vs. Night  $P = 0.0134$ , KI Day vs. Night  $P = 0.0004$ , Night Con vs. KI  $P = 0.011$ , Day Con vs. KI  $P = 0.0424$ ; systolic BP: Con Day vs. Night  $P = 0.1009$ , KI Day vs. Night  $P = 0.0037$ , Night Con vs. KI  $P = 0.033$ , Day Con vs. KI  $P = 0.1734$ ; diastolic BP: Con Day vs. Night  $P = 0.0038$ , KI Day vs. Night  $P = 0.0001$ , Night Con vs. KI  $P = 0.0056$ , Day Con vs. KI  $P = 0.0147$ ; HR: Con Day vs. Night  $P = 0.0008$ , KI Day vs. Night  $P < 0.0001$ , Night Con vs. KI  $P = 0.0013$ , Day Con vs. KI  $P = 0.0014$ ; activity: Con Day vs. Night  $P = 0.013$ , KI Day vs. Night  $P < 0.0001$ , Night Con vs. KI  $P = 0.2862$ , Day Con vs. KI  $P = 0.5970$ ; body temperature: Con Day vs. Night  $P = 0.0113$ , KI Day vs. Night  $P = 0.0162$ , Night Con vs. KI  $P = 0.563$ , Day Con vs. KI  $P = 0.743$ ). G, summary time course of AngII-induced hypertension development using systolic blood pressure (BP) recorded by tail cuff plethysmography at day 0 (before AngII), 7 and 14 (means  $\pm$  SD,  $n = 6$ , unpaired  $t$ -test, 7 days post-AngII  $P = 0.0004$ ). H, vascular tension in response to KCl (90 mM) in mesenteric artery segments using wire myography from normotensive (N) and hypertensive mice (H) (means  $\pm$  SD;  $n = 6–9$ , ANOVA with Fisher's LSD test: ConKI N vs. H  $P = 0.0069$ , N ConKI vs. KI  $P = 0.4817$ , H ConKI vs. KI  $P = 0.1932$ , KI N vs. H  $P = 0.0446$ ). I, acetylcholine (ACh)-induced relaxation recorded as percentage of relaxation in response to cumulative concentrations of ACh (means  $\pm$  SD,  $n = 3–7$ , ANOVA, not significant). J, sodium nitroprusside (SNP)-induced relaxation was recorded as percentage of relaxation in response to cumulative concentrations of SNP in the 4 groups (means  $\pm$  SD;  $n = 4–7$ , ANOVA, ns). [Colour figure can be viewed at [wileyonlinelibrary.com](http://wileyonlinelibrary.com)]

To further assess potential transcriptional remodelling in the vasculature and heart that may underlie the tachycardia and hypertension phenotypes, we performed RNA seq analyses on the aorta and the heart. Pathway enrichment analyses of DEGs between the two genotypes showed downregulation of the TCA cycle and electron transport chain in the KI in the aorta (Fig. 6E). This downregulation may be expected to lower VSM contractility, which was not observed in the functional studies. Also, downregulation of fatty acid  $\beta$ -oxidation was noted (Fig. 6E). In the heart no notable pathways that may readily explain the increased heart rate or indicate

potential heart defects were enriched or downregulated (Fig. 6F).

Mean arterial blood pressure (MAP) in the systemic circulation is a function of total peripheral vascular resistance (TPR) and cardiac output (CO) ( $\text{MAP} = \text{TPR} \times \text{CO}$ ) (Drummond et al., 2019). Cardiac output is the product of heart rate and stroke volume ( $\text{CO} = \text{HR} \times \text{SV}$ ), and therefore an increased HR would lead to increased BP. Having ruled out VSM contractility and arterial wall remodelling as contributors to the hypertension in the hypomorph, we next focused on the increased HR.

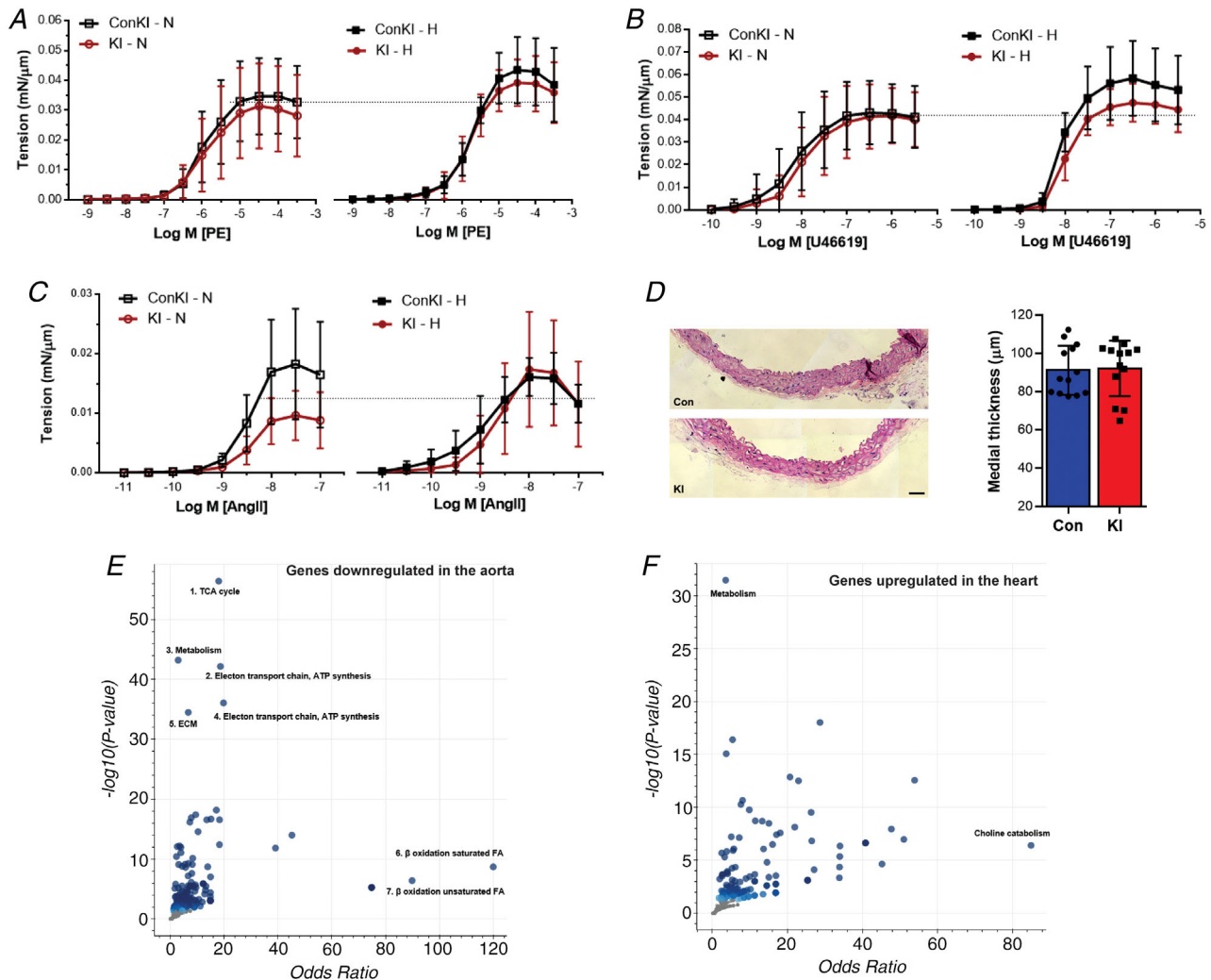


**Figure 6. Cardiovascular pathologies in the STIM1 hypomorph**

A–C, contractile responses of mesenteric arteries in response to a phenylephrine (PE) (A), U46619 (B) or AngII (C) dose response (means  $\pm$  SD;  $n = 5-9$ , ANOVA, not significant). D, left, representative H&E-stained descending aorta sections. Scale bar is 50  $\mu\text{m}$ . Right, quantification of thickness of aorta smooth muscle layer (means  $\pm$  SD;  $n = 13$ , unpaired  $t$ -test,  $P = 0.8593$ ). E and F, pathway enrichment analysis of differentially expressed genes in aorta (E) or heart (F) using ENRICH (maayanlab.cloud/Enrichr). Graphs were generated using appyters (appyters.maayanlab.cloud). For aorta only downregulated pathways in the hypomorph are shown with no significant upregulated pathways identified. For the heart only upregulated pathways are shown as no significant downregulated pathways were identified. For both aorta and heart, RNA was isolated from four mice each for the ConKI and KI, of mixed sexes two males and two females. No sex-specific differences were noted. [Colour figure can be viewed at [wileyonlinelibrary.com](http://wileyonlinelibrary.com)]

STIM1 has been shown to be important for SAN function (Zhang et al., 2015), raising the possibility that the tachycardia observed in the hypomorph is due to a heart-specific SOCE defect. To test for this possibility, we generated a heart-specific STIM1 hypomorph by crossing the ConKI with an  $\alpha$ MHC-cre line. This leads to expression of the long STIM1 only in the heart and WT STIM1 in the rest of the tissues as confirmed by western blots using two different STIM1 antibodies (Fig. 7A) that we have previously validated (Yu et al., 2019). Surprisingly and despite the documented role of STIM1 in the SAN (Zhang et al., 2015), heart-specific KI animals had a normal heart rate similar to that observed in ConKI animals and lower than in whole body KI mice (Fig. 7B). These data argue that the tachycardia observed in KI mice is not due to SOCE function in the heart, but rather to lower SOCE in other tissues.

HR is modulated by the autonomic nervous system to maintain homeostasis. Analysis of heart rate variability

(HRV) offers a non-invasive approach to assess the balance of sympathetic and parasympathetic systems. We performed HRV analyses in the frequency and time domains as described by others (Laude et al., 2008; Thireau et al., 2008), to determine whether there are alterations in autonomic nervous system function in the hypomorph. In the frequency domain the low frequency power spectrum (LF) reflects sympathetic activity, whereas the high frequency spectrum (HF) reflects parasympathetic activity. We observe an increased sympathetic activity as reflected in the LF spectrum in the hypomorph as compared to control animals (Fig. 7C), with no change in parasympathetic activity in the HF domain (Fig. 7C). In the time domain we assessed the standard deviation of normal-to-normal R-R peak intervals (SDNN), which reflects total autonomic variability; the root mean square of successive differences between normal heartbeats (RMSSD), which reflects short term HR variability; and the percentage of normal consecutive

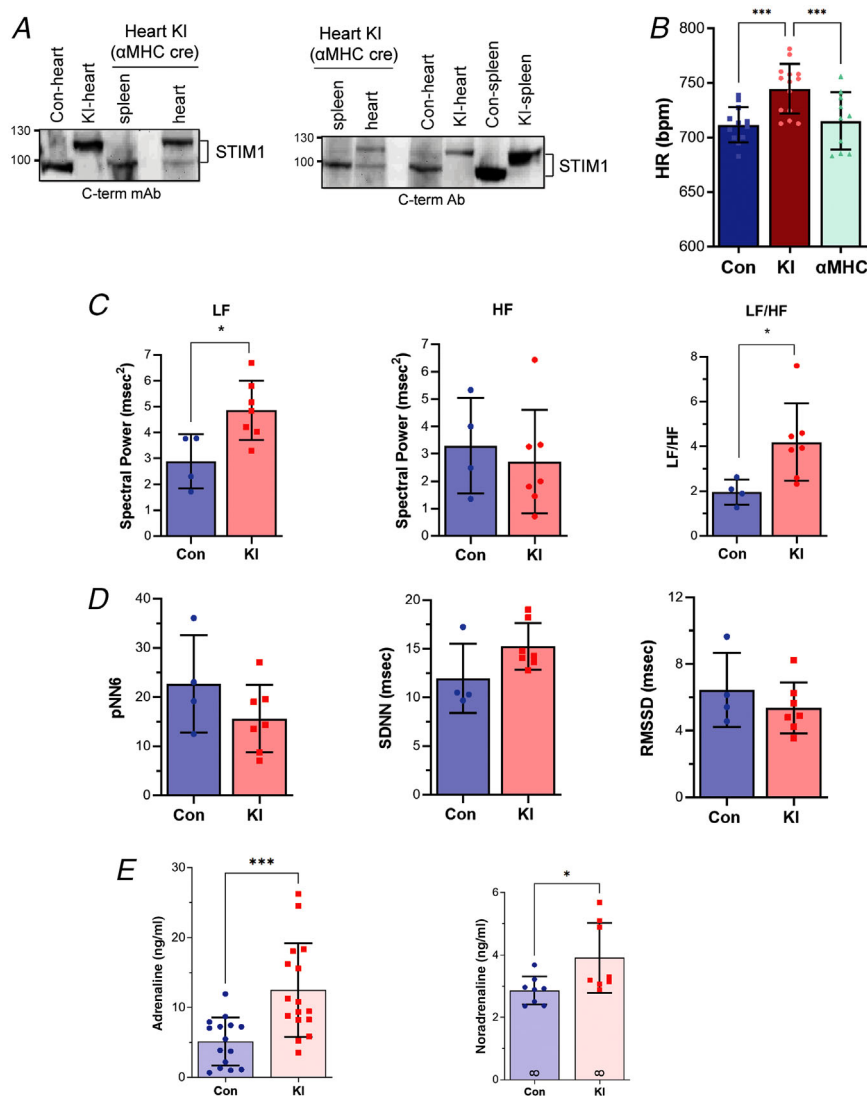


**Figure 7. Tachycardia in hypomorph mice due to increased catecholamines**  
 A, left, western blot of STIM1 in spleen and heart tissues from the heart-specific KI ( $\alpha$ MHC-Cre), ConKI and KI mice. Faint band of lower STIM1 in heart-specific KI is due to contamination of blood cells. Right, western blot of STIM1 in spleen and heart tissues from the heart-specific KI ( $\alpha$ MHC-Cre), ConKI and KI mice. B, heart rate (HR) measured by non-invasive footpad electrodes to record ECG (means  $\pm$  SD,  $n = 10$ –14, ANOVA: ConKI vs. KI  $P = 0.001$ , ConKI vs.  $\alpha$ MHC  $P = 0.7077$ ). C and D, heart rate variability analyses of telemetry ECG data in the frequency (C) and time domains (D) in ConKI and KI mice (means  $\pm$  SD;  $n = 4$ –7, unpaired  $t$ -test, ConKI vs. KI: LF  $P = 0.0199$ , HF  $P = 0.6275$ , LF/HF  $P = 0.0675$ , pNN6  $P = 0.1941$ , SDNN  $P = 0.0953$ , RMSSD  $P = 0.3651$ ). E, catecholamine levels in plasma from ConKI and KI mice (means  $\pm$  SD;  $n = 16$  for Adrenaline and 8 for Noradrenaline, unpaired  $t$ -test, ConKI vs. KI: Adrenaline  $P = 0.0007$ , Noradrenaline  $P = 0.0286$ ). [Colour figure can be viewed at [wileyonlinelibrary.com](http://wileyonlinelibrary.com)]

R–R intervals differing by  $>6$  ms (pNN6), which reports cardiac parasympathetic activity. We observed no differences in these parameters between the two strains (Fig. 7D), supporting the finding from the frequency domain analysis of no change in parasympathetic activity in the hypomorph. These data argue that the STIM1 hypomorph exhibits higher levels of basal sympathetic autonomic nervous system activity.

To independently test this conclusion, we measured the levels of adrenaline and noradrenaline in plasma as both are secreted in response to sympathetic activity (Young & Davisson, 2011). Indeed, we observed increased levels of circulating adrenaline and noradrenaline in the KI as compared to ConKI animals (Fig. 7E). These results support the conclusions from the HRV analyses and argue that STIM1 hypomorph animals exhibit increased sympathetic activity which underlies the observed tachycardia and hypertensive phenotypes.

## Discussion

To determine whether chronic SOCE inhibition is viable therapeutically, we dissected pathologies associated with chronic inhibition of SOCE using a novel mouse genetic model with significantly decreased SOCE. The decrease in SOCE and SOCE-dependent signalling including NFAT nuclear translocation and cytokine production was consistently 65–75%. This SOCE hypomorph phenotype is due to the expression of a long chimeric STIM1 protein with a duplicated portion of the C-terminal end of the protein. Chimeric STIM1 does not translocate efficiently to ER–PM membrane-contact sites resulting in a significant reduction in STIM1 puncta density following store depletion. This reduction leads to decreased Orail recruitment and gating and thus less  $\text{Ca}^{2+}$  entry through SOCE.

We show that SOCE hypomorph mice are fertile and reproduce and develop normally. They do, however, develop hypertension and tachycardia. Our data argue that the hypertension observed in the hypomorph is due to the tachycardia as we could not detect any significant changes in vascular remodelling, VSM contractility, or relevant transcriptional remodelling in either the heart or the aorta in the hypomorph. We further show that hypomorph mice have increased sympathetic activity as reflected in HRV analyses and increased circulating catecholamines, which would explain the tachycardia.

Mice with the VSM-specific STIM1 knockout exhibit increased HR and sympathetic activity (Pichavaram et al., 2018), similar to what we observe in the hypomorph. This argues that SOCE downregulation may be mediating increased sympathetic activity by acting in multiple organs, including the vasculature and potentially

the central nervous system. Recently, acute STIM1 deletion in VSM has been shown to decrease contractility and result in hypotension in mice (Krishnan et al., 2022). Interestingly, Krishnan et al. argue that the loss of STIM1 mediates these pathologies in an SOCE-independent fashion, because STIM1 is constitutively clustered in contractile VSM with little functional SOCE. These results support our findings of the absence of an effect on VSM contractility in the hypomorph despite the lower SOCE levels and argue that in the hypomorph the STIM1-dependent SOCE-independent functions are maintained.

SOCE and STIM1 in particular have been implicated in various cardiovascular pathologies including, among others, cardiac hypertrophy (Hulot et al., 2011; Ohba et al., 2009); fibrosis, ER stress, and mitochondria dysfunction (Collins et al., 2014; Collins et al., 2022); hypertension (Kassan et al., 2016); arrhythmias (Cacheux et al., 2019); and remodelling of the vasculature (Bisaillon et al., 2010; Zhang et al., 2011). Many of these studies have used tissue-specific STIM1 knockout models. In contrast, our hypomorph model is a partial SOCE loss of function that exhibits different and as expected milder pathologies. Specifically, decreasing SOCE function in the heart only using a heart-specific SOCE hypomorph line ( $\alpha\text{MHC}$ -cre hypomorph) does not lead to tachycardia. Importantly,  $\alpha\text{MHC}$  (*Myh6* gene) is expressed in SAN cells (Galang et al., 2020). Complete deletion of STIM1 in the SAN has been shown to decrease  $\text{Ca}^{2+}$  store content and spontaneous  $\text{Ca}^{2+}$  transients, with an associated decreased heart rate (Zhang et al., 2015). In contrast in the hypomorph, which is a partial loss of function of STIM1, we observe an increased HR due to increased sympathetic activity. This argues that either the residual STIM1 function in the hypomorph is sufficient to maintain SAN rhythmicity or that the enhanced sympathetic activity overshadows the effect at the SAN level.

In conclusion, chronic SOCE inhibition is a viable anti-inflammatory approach but would need to be considered with caution given the associated cardiovascular complications. Importantly, SOCE hypomorph mice are not susceptible to diabetes development and they develop and reproduce normally. Finally, the SOCE hypomorph model allows for organ-specific dissection of potential pathologies and functions of SOCE.

## References

- Agah, R., Frenkel, P. A., French, B. A., Michael, L. H., Overbeek, P. A., & Schneider, M. D. (1997). Gene recombination in postmitotic cells. Targeted expression of Cre recombinase provokes cardiac-restricted, site-specific rearrangement in adult ventricular muscle in vivo. *Journal of Clinical Investigation*, **100**(1), 169–179.



- Azzi, J. R., Sayegh, M. H., & Mallat, S. G. (2013). Calcineurin inhibitors: 40 years later, can't live without. *Journal of Immunology*, **191**(12), 5785–5791.
- Bamgbola, O. (2016). Metabolic consequences of modern immunosuppressive agents in solid organ transplantation. *Therapeutic Advances in Endocrinology and Metabolism*, **7**(3), 110–127.
- Bisaillon, J. M., Motiani, R. K., Gonzalez-Cobos, J. C., Potier, M., Halligan, K. E., Alzawahra, W. F., Barroso, M., Singer, H. A., Jourdeuil, D., & Trebak, M. (2010). Essential role for STIM1/Orai1-mediated calcium influx in PDGF-induced smooth muscle migration. *American Journal of Physiology. Cell Physiology*, **298**(5), C993–C1005.
- Cacheux, M., Strauss, B., Raad, N., Ilkan, Z., Hu, J., Benard, L., Feske, S., Hulot, J. S., & Akar, F. G. (2019). Cardiomyocyte-specific STIM1 (stromal interaction molecule 1) depletion in the adult heart promotes the development of arrhythmogenic discordant alternans. *Circulation: Arrhythmia and Electrophysiology*, **12**(11), e007382.
- Chakkerla, H. A., Kudva, Y., & Kaplan, B. (2017). Calcineurin inhibitors: Pharmacologic mechanisms impacting both insulin resistance and insulin secretion leading to glucose dysregulation and diabetes mellitus. *Clinical Pharmacology & Therapeutics*, **101**(1), 114–120.
- Chen, E. Y., Tan, C. M., Kou, Y., Duan, Q., Wang, Z., Meirelles, G. V., Clark, N. R., & Ma'ayan, A. (2013). Enrichr: Interactive and collaborative HTML5 gene list enrichment analysis tool. *BMC Bioinformatics*, **14**(1), 128.
- Collins, H. E., Anderson, J. C., Wende, A. R., & Chatham, J. C. (2022). Cardiomyocyte stromal interaction molecule 1 is a key regulator of  $\text{Ca}^{2+}$ -dependent kinase and phosphatase activity in the mouse heart. *Physiological Reports*, **10**(4), e15177.
- Collins, H. E., He, L., Zou, L., Qu, J., Zhou, L., Litovsky, S. H., Yang, Q., Young, M. E., Marchase, R. B., & Chatham, J. C. (2014). Stromal interaction molecule 1 is essential for normal cardiac homeostasis through modulation of ER and mitochondrial function. *American Journal of Physiology. Heart and Circulatory Physiology*, **306**(8), H1231–H1239.
- Drummond, G. R., Vinh, A., Guzik, T. J., & Sobey, C. G. (2019). Immune mechanisms of hypertension. *Nature Reviews Immunology*, **19**(8), 517–532.
- Estrada, I. A., Donthamsetty, R., Debski, P., Zhou, M. H., Zhang, S. L., Yuan, J. X., Han, W., & Makino, A. (2012). STIM1 restores coronary endothelial function in type 1 diabetic mice. *Circulation Research*, **111**(9), 1166–1175.
- Feske, S., Wulff, H., & Skolnik, E. Y. (2015). Ion channels in innate and adaptive immunity. *Annual Review of Immunology*, **33**(1), 291–353.
- Galang, G., Mandla, R., Ruan, H., Jung, C., Sinha, T., Stone, N. R., Wu, R. S., Mannion, B. J., Allu, P. K. R., Chang, K., Rammohan, A., Shi, M. B., Pennacchio, L. A., Black, B. L., & Vedantham, V. (2020). ATAC-seq reveals an *isl1* enhancer that regulates sinoatrial node development and function. *Circulation Research*, **127**(12), 1502–1518.
- Gwack, Y., Srikanth, S., Oh-hora, M., Hogan, P. G., Lamperti, E. D., Yamashita, M., Gelinis, C., Neems, D. S., Sasaki, Y., Feske, S., Prakriya, M., Rajewsky, K., & Rao, A. (2008). Hair loss and defective T- and B-cell function in mice lacking Orai1. *Molecular and Cellular Biology*, **28**, 5209–5222.
- Hammad, A. S., Yu, F., Botheju, W. S., Elmi, A., Alcantara-Adap, E., & Machaca, K. (2021). Phosphorylation of STIM1 at ERK/CDK sites is dispensable for cell migration and ER partitioning in mitosis. *Cell Calcium*, **100**, 102496.
- Hartono, C., Muthukumar, T., & Suthanthiran, M. (2013). Immunosuppressive drug therapy. *Cold Spring Harbor Perspectives in Medicine*, **3**(9), a015487.
- Hogan, P. G., Lewis, R. S., & Rao, A. (2010). Molecular basis of calcium signaling in lymphocytes: STIM and Orai. *Annual Review of Immunology*, **28**, 491–533.
- House, S. J., Potier, M., Bisaillon, J., Singer, H. A., & Trebak, M. (2008). The non-excitable smooth muscle: Calcium signaling and phenotypic switching during vascular disease. *Pflügers Archiv: European Journal of Physiology*, **456**(5), 769–785.
- Hulot, J. S., Fauconnier, J., Ramanujam, D., Chaanine, A., Aubart, F., Sassi, Y., Merkle, S., Cazorla, O., Ouille, A., Dupuis, M., Hadri, L., Jeong, D., Muhlstedt, S., Schmitt, J., Braun, A., Benard, L., Saliba, Y., Lagerbauer, B., Nieswandt, B., Lacampagne, A., Hajjar, R. J., Lompre, A. M., & Engelhardt, S. (2011). Critical role for stromal interaction molecule 1 in cardiac hypertrophy. *Circulation*, **124**(7), 796–805.
- Kabata, H., Flamar, A. L., Mahlakoiv, T., Moriyama, S., Rodewald, H. R., Ziegler, S. F., & Artis, D. (2020). Targeted deletion of the TSLP receptor reveals cellular mechanisms that promote type 2 airway inflammation. *Mucosal Immunology*, **13**(4), 626–636.
- Kassan, M., Ait-Aissa, K., Radwan, E., Mali, V., Haddox, S., Gabani, M., Zhang, W., Belmadani, S., Irani, K., Trebak, M., & Matrougui, K. (2016). Essential role of smooth muscle STIM1 in hypertension and cardiovascular dysfunction. *Arteriosclerosis, Thrombosis, and Vascular Biology*, **36**(9), 1900–1909.
- Kono, T., Tong, X., Taleb, S., Bone, R. N., Iida, H., Lee, C. C., Sohn, P., Gilon, P., Roe, M. W., & Evans-Molina, C. (2018). Impaired store-operated calcium entry and STIM1 loss lead to reduced insulin secretion and increased endoplasmic reticulum stress in the diabetic beta-cell. *Diabetes*, **67**(11), 2293–2304.
- Kontgen, F., Suss, G., Stewart, C., Steinmetz, M., & Bluethmann, H. (1993). Targeted disruption of the MHC class II Aa gene in C57BL/6 mice. *International Immunology*, **5**(8), 957–964.
- Krishnan, V., Ali, S., Gonzales, A. L., Thakore, P., Griffin, C. S., Yamasaki, E., Alvarado, M. G., Johnson, M. T., Trebak, M., & Earley, S. (2022). STIM1-dependent peripheral coupling governs the contractility of vascular smooth muscle cells. *eLife*, **11**.
- Kuleshov, M. V., Jones, M. R., Rouillard, A. D., Fernandez, N. F., Duan, Q., Wang, Z., Koplev, S., Jenkins, S. L., Jagodnik, K. M., Lachmann, A., McDermott, M. G., Monteiro, C. D., Gundersen, G. W., & Ma'ayan, A. (2016). Enrichr: A comprehensive gene set enrichment analysis web server 2016 update. *Nucleic Acids Research*, **44**(W1), W90–W97.
- Lacruz, R. S., & Feske, S. (2015). Diseases caused by mutations in Orai1 and STIM1. *Annals of the New York Academy of Sciences*, **1356**(1), 45–79.

- Laude, D., Baudrie, V., & Elghozi, J. L. (2008). Applicability of recent methods used to estimate spontaneous baroreflex sensitivity to resting mice. *American Journal of Physiology. Regulatory, Integrative and Comparative Physiology*, **294**(1), R142–R150.
- Mamenko, M., Dhande, I., Tomilin, V., Zaika, O., Boukelmoune, N., Zhu, Y., Gonzalez-Garay, M. L., Pochynyuk, O., & Doris, P. A. (2016). Defective store-operated calcium entry causes partial nephrogenic diabetes insipidus. *Journal of the American Society of Nephrology*, **27**(7), 2035–2048.
- Oh-Hora, M., Yamashita, M., Hogan, P. G., Sharma, S., Lamperti, E., Chung, W., Prakriya, M., Feske, S., & Rao, A. (2008). Dual functions for the endoplasmic reticulum calcium sensors STIM1 and STIM2 in T cell activation and tolerance. *Nature Immunology*, **9**(4), 432–443.
- Ohba, T., Watanabe, H., Murakami, M., Sato, T., Ono, K., & Ito, H. (2009). Essential role of STIM1 in the development of cardiomyocyte hypertrophy. *Biochemical and Biophysical Research Communications*, **389**(1), 172–176.
- Orie, N. N., Fry, C. H., & Clapp, L. H. (2006). Evidence that inward rectifier  $\text{K}^{+}$  channels mediate relaxation by the  $\text{PGI}_2$  receptor agonist cicaprost via a cyclic AMP-independent mechanism. *Cardiovascular Research*, **69**(1), 107–115.
- Park, C. Y., Hoover, P. J., Mullins, F. M., Bachhawat, P., Covington, E. D., Raunser, S., Walz, T., Garcia, K. C., Dolmetsch, R. E., & Lewis, R. S. (2009). STIM1 clusters and activates CRAC channels via direct binding of a cytosolic domain to Orai1. *Cell*, **136**(5), 876–890.
- Picard, C., McCarl, C. A., Papolos, A., Khalil, S., Luthy, K., Hivroz, C., LeDeist, F., Rieux-Laucat, F., Rechavi, G., Rao, A., Fischer, A., & Feske, S. (2009). STIM1 mutation associated with a syndrome of immunodeficiency and autoimmunity. *New England Journal of Medicine*, **360**(19), 1971–1980.
- Pichavaram, P., Yin, W., Evanson, K. W., Jaggar, J. H., & Mancarella, S. (2018). Elevated plasma catecholamines functionally compensate for the reduced myogenic tone in smooth muscle STIM1 knockout mice but with deleterious cardiac effects. *Cardiovascular Research*, **114**(5), 668–678.
- Prakriya, M., & Lewis, R. S. (2015). Store-operated calcium channels. *Physiological Reviews*, **95**(4), 1383–1436.
- Stauderman, K. A. (2018). CRAC channels as targets for drug discovery and development. *Cell Calcium*, **74**, 147–159.
- Thireau, J., Zhang, B. L., Poisson, D., & Babuty, D. (2008). Heart rate variability in mice: A theoretical and practical guide. *Experimental Physiology*, **93**(1), 83–94.
- Vaeth, M., Kahlfuss, S., & Feske, S. (2020). CRAC channels and calcium signaling in T cell-mediated immunity. *Trends in Immunology*, **41**(10), 878–901.
- Vig, M., DeHaven, W. I., Bird, G. S., Billingsley, J. M., Wang, H., Rao, P. E., Hutchings, A. B., Jouvin, M. H., Putney, J. W., Jr., & Kinet, J. P. (2008). Defective mast cell effector functions in mice lacking the CRACM1 pore subunit of store-operated calcium release-activated calcium channels. *Nature Immunology*, **9**, 89–96.
- Young, C. N., & Davisson, R. L. (2011). In vivo assessment of neurocardiovascular regulation in the mouse: Principles, progress, and prospects. *American Journal of Physiology. Heart and Circulatory Physiology*, **301**(3), H654–H662.
- Yu, F., Agrebi, N., Mackeh, R., Abouhazima, K., KhudaBakhsh, K., Adeli, M., Lo, B., Hassan, A., & Machaca, K. (2021). Novel ORAI1 mutation disrupts channel trafficking resulting in combined immunodeficiency. *Journal of Clinical Immunology*, **41**(5), 1004–1015.
- Yu, F., Hubrack, S. Z., Chakraborty, S., Sun, L., Alcantara-Adap, E., Kulkarni, R., Billing, A. M., Graumann, J., Taylor, C. W., & Machaca, K. (2019). Remodeling of ER-plasma membrane contact sites but not STIM1 phosphorylation inhibits  $\text{Ca}^{2+}$  influx in mitosis. *Proceedings of the National Academy of Sciences, USA*, **116**(21), 10392–10401.
- Yu, F., Sharma, S., Jankovic, D., Gurram, R. K., Su, P., Hu, G., Li, R., Rieder, S., Zhao, K., Sun, B., & Zhu, J. (2018). The transcription factor Bhlhe40 is a switch of inflammatory versus antiinflammatory Th1 cell fate determination. *Journal of Experimental Medicine*, **215**(7), 1813–1821.
- Zhang, H., Sun, A. Y., Kim, J. J., Graham, V., Finch, E. A., Nepliouev, I., Zhao, G., Li, T., Lederer, W. J., Stiber, J. A., Pitt, G. S., Bursac, N., & Rosenberg, P. B. (2015). STIM1- $\text{Ca}^{2+}$  signaling modulates automaticity of the mouse sinoatrial node. *Proceedings of the National Academy of Sciences, USA*, **112**(41), E5618–E5627.
- Zhang, W., Halligan, K. E., Zhang, X., Bisailon, J. M., Gonzalez-Cobos, J. C., Motiani, R. K., Hu, G., Vincent, P. A., Zhou, J., Barroso, M., Singer, H. A., Matrougui, K., & Trebak, M. (2011). Orai1-mediated I (CRAC) is essential for neointima formation after vascular injury. *Circulation Research*, **109**(5), 534–542.

## Additional information

### Data availability statement

All data reported are included in the manuscript proper and are available on request.

### Competing interests

The authors declare that the research was conducted in the absence of any commercial or financial relationships that could be construed as a potential conflict of interest.

### Author contributions

K. M. designed the study, procured funding, analyzed data, prepared figures, and wrote the manuscript. F. Y. and R. C. contributed to conception of the work, acquisition, analysis, and interpretation of the data. A. E., E. A. A., N. N. O., F. Z., S. H., S. W. performed experiments, acquired and analyzed data. S. H., N. A., S. W., M. S., V. M. A. contributed to training and/or data interpretation. All authors have read and approved the final version of this manuscript and agree to be accountable for all

aspects of the work in ensuring that questions related to the accuracy or integrity of any part of the work are appropriately investigated and resolved. All persons designated as authors qualify for authorship, and all those who qualify for authorship are listed.

### Funding

This work as well as the Cores are supported by the Biomedical Research Program at Weill Cornell Medical College in Qatar (BMRP), a program funded by Qatar Foundation. This work was also funded by a grant from the Qatar National Research Fund (QNRF), grant number NPRP12S-0212-190074. The statements made herein are solely the responsibility of the authors. Open access funding provided by the Qatar National Library.

### Acknowledgements

The authors are grateful to Stefan Feske (NYU) for the STIM1flox/flox mouse line, and to Masatsugu Oh-hora (Tokyo Medical and Dental University) for the STIM1-KO MEF cell line. The authors thank the Vivarium, Microscopy, Genomics, and Bioinformatics Cores at WCMQ for their support in

multiple experiments. Open access funding provided by the Qatar National Library.

### Authors' present address

A. Elmi and S. Hubrack: SIDRA Medicine, Doha, Qatar.

### Keywords

hypertension, immunodeficiency, STIM1, store-operated  $\text{Ca}^{2+}$  entry, tachycardia

### Supporting information

Additional supporting information can be found online in the Supporting Information section at the end of the HTML view of the article. Supporting information files available:

**Statistical Summary Document**

**Peer Review History**